Title

Solid-state Nuclear Magnetic Resonance Studies of Secondary Plant Cell Wall Polymer Arrangement: Mechanically Induced Recalcitrance Markers in Sorghum bicolor

Author

Munson, Coyla Rachel

Publication Date

2022

Peer reviewed|Thesis/dissertation

Solid-state Nuclear Magnetic Resonance Studies of Secondary Plant Cell Wall Polymer Arrangement: Mechanically Induced Recalcitrance Markers in *Sorghum bicolor*

By

COYLA R MUNSON

THESIS

Submitted in partial satisfaction of the requirements for the degree of

MASTER OF SCIENCE

in

Chemistry

in the

OFFICE OF GRADUATE STUDIES

of the

UNIVERSITY OF CALIFORNIA

DAVIS

Approved:

Dylan T. Murray, Chair

Jim Ames

Gang-yu Liu

Committee in Charge

2022

Acknowledgements

Sections of this work are adapted and expanded upon from Munson *et al.* 2022. This work could not have been possible without the support from the Murray lab, family, and dear collaborators from the Mortimer lab. I would like to especially thank Dr. Jenny Mortimer for their guidance and expertise in plant biomass and the secondary plant cell wall and her postdoc Dr. Yu Gao who grew the *Sorghum bicolor*. Dr. Dylan Murray deserves a special shout out for introducing me and helping to form my knowledge of solid-state NMR. Interdisciplinary guidance from the Mortimer Lab and Dr. Dylan Murray helped to outline the understanding culminated in this work and the vast literature on the emerging topic of probing plant biomass for biofuels using solid-state NMR.

Abstract

Unlocking one third of plant biomass as a renewable feedstock for fuels and materials depends on the effective deconstruction of the secondary plant cell wall. Over 90% of the native secondary plant cell wall is composed of cellulose and hemicellulose polysaccharides and the lignin heteroaromatic polymers. Deconstruction refers to the processes which digest polymers into desired subunits. Present deconstruction processes are centered on lignin-first extraction to overcome the recalcitrance of biomass: the accumulation of indigestible plant polymers during deconstruction. Recent availability of ^{13}C-enriched plant biomass has enabled the use of solid-state Nuclear Magnetic Resonance (NMR) experiments to refine the model of native cell wall structure in plant tissue in biofuel relevant crops. Solid-state NMR has the advantageous ability to non-invasively probe the structure of the secondary plant cell wall throughout deconstruction pathways and potentially refine methods development for the conversion of plant biomass to sustainable products. The mechanical preprocessing of plant material to solubilize the plant cell wall could introduce recalcitrance at the beginning of the deconstruction pathway. In this research solid-state NMR of *Sorghum bicolor* stems mechanically preprocessed on the lab scale (by vibratory ballmilling at 30 Hz for 2 and 15 minutes) supported recalcitrant reorganization in lignin and hemicellulose. Recalcitrance related to lignin becoming more rigid, potentially trapping other polymers was supported by a reduction in highly dynamic signals of arabinosyl hemicellulose (correlated in lignin-hemicellulose cross linkages), lignin linkages, and lignin probed in the refocused Incredible Nuclear Enhancement by Polarization Transfer (rINEPT) experiment. Cross polarized experiments targeting rigid polymers supported potential recalcitrance from structural hemicellulose as signals: which persisted after milling at a greater signal intensity than cellulose. Recalcitrance from cellulose polymers converting from crystalline to amorphous cellulose as fibril structures are broken down was not supported here, the cellulose carbon 4 peaks was a valuable marker for identifying morphology changes for the cellulose fibril along with scanning electron microscopy.

Table of Contents

Acknowledgements II
Abstract III
Table of Figures VI
Chapter 1: Introduction 1
Unlocking One Third of Plant biomass: Applications for the Secondary Plant Cell Wall 1
Challenges Accessing the Secondary Plant Cell Wall Polymers: Insolubility and Recalcitrance 1
Cost Effective ^{13}C Labeling Enables Structural Insight into Secondary Plant Cell Wall by Solid-state NMR 2
Chemical Composition and Organization of the Secondary Plant Cell Wall 4
The Secondary Plant Cell Wall: Arrangement of the World's Naturally Abundant Polymers 4
Advances Toward an Accurate 3D Model for the Native Plant Cell Wall Using Solid-State NMR 7
Chapter 2: Studying Mechanically Induced Recalcitrance 11
Recalcitrance of the Secondary Plant Cell Wall Proposed from Mechanical Preprocessing 11
Advancements in Overcoming Plant Cell Wall Recalcitrance 12
Recalcitrance Reintroduced During Deconstruction Techniques of Biomass 13
Tracking Mechanically Induced Recalcitrance 14
Markers of Recalcitrance Hypothesized for Ball-milling from Literature 16
Evaluation of Recalcitrance Markers in 2D Solid-state NMR Experiments: Chemical Shifts and Integration 18
Chapter 3: Methods 20
Growth of the ^{13}C Labeled Plant Material 20
Sample Preparation of Sorghum Stems 20
Milling Conditions of Plant Materials 20
Sample Morphology Tracked with FE-SEM 21
Atomic Resolution of Sorghum Stem Secondary Plant Cell Wall by MAS-ssNMR 21
Chapter 4: Results and Discussion 24
Monitoring Secondary Plant Cell Wall Reorganization During Ball-Milling 24
Cellulose Fibril Changes During Milling 25
Cellulose Fibril Morphological Changes 25
Atomic Changes in Cellulose Fibril Structure 27
Hemicellulose Changes After Milling 35
Structural Hemicellulose Changes After Milling 35

Dynamic Hemicellulose Changes During Milling 37
Lignin Changes in the Plant Cell Wall Matrix During Milling 39
Mechanically Induced Milling Recalcitrance by Vibratory Milling 41
Chapter 5: Outlook and Conclusion 41
Bibliography 45
Appendix 53

Table of Figures

Figure 1. An introduction to secondary plant cell wall biomass conversion into bioproducts (A), structure (B), and testing for mechanically induced recalcitrance (C). Plant biomass secondary plant cell wall is highlighted and a general scheme of secondary plant cell wall conversion (preprocessing and polymer deconstruction) to bioproducts (A). A generalized diagram of the secondary plant cell wall polymers from the structural insights of previous works is outlined here,[1,23,24] and recalcitrance as an impediment to depolymerization to bioproducts[22] (B). Solid-state NMR is used to test mechanical preprocessing as a source of secondary plant cell wall recalcitrance on the lab scale with minimal additional sample manipulation (C). The advancement of $^{13}CO_2$ labeling and stem tissue enables multidimensional NMR to contrast a cut stem control with milled samples.[24–27] 2

Figure 2. Work from previous literature is summarized to create a current diagram of cellulose in the secondary plant cell wall. The cellulose monomer is made of D-glucose monomers (A) and the polymer (B) is made up of β-(1,4)-glucan. Within the crystallite sheets are the individual cellulose polymer chains which hydrogen bond laterally (orange),[20,52] so when the sheets stacks together they form hydrophilic and hydrophobic surfaces (C).[1,56]Each microfibril contains crystallite sheets held together with dispersion forces from the hydrophobic faces of the sugars (D).[1,57] The cellulose fibril is composed of a collection of microfibrils (E).[1] 5

Figure 3. Structural hemicellulose monomers including xylose(A), D-galactose(B), D-mannose(C), and D-glucose(D) from polymers contain main chain linear with 1-O-4 linkages and some arabinose(E), acetylations and other decorations are excluded here and better encapsulated in Scheller and Ulvskov 2010 and Gao et al 2020. In sorghum, xylan is the prominent structural hemicellulose with irregular, prominent arabinosyl groups which can crosslink to lignin as exemplified in panel F.[10,24,60] In the secondary plant cell wall xylan hemicellulose interacts with amorphous and crystalline cellulose (G).[24] Xylan takes on a 2-fold screw axis morphology (^{2f}Xylan) along the polymer axis when it associates with crystalline cellulose surfaces (G, H).[23,24] Unbound and xylan associating to amorphous cellulose takes on a 3-fold screw axis along the polymer axis (^{3f}Xylan) (G,H).[23,24,58] 6

Figure 4. The heteroaromatic polymer (lignin) comprises 15-20% of the sorghum plant cell wall,[1,7,24] and is composed of monolignols and here the aromatic rings are color coded Ferulic Acid (FA) in pink(A), Hydroxyphenyl (H) in orange(B), Guaiacyl (G) in yellow(C), and Syringyl (S) in green(D). There are nine lignin linkages, only eight linkages are shown and the 4-5 linkage was excluded for simplicity (E). The β-O-4, β-5, β-β, spirodienone β-1 linkages are the most common in sorghum.[7] 7

Figure 5. The proposed mechanical induced recalcitrance scheme in panel A can be broken down by recalcitrance from each polymer. These original schemes summarize findings from previous literature. Cellulose conversion from crystalline to amorphous cellulose is a reported source of recalcitrance (B).[5,54,84] Structural hemicellulose further associating with cellulose surfaces or increasing cross-linkages between xylan and lignin noted in Terrett and Dupree 2019 and given ^{3f,A}Xylan and ^{3f}Xylan both associate with amorphous cellulose in sorghum as discovered in Gao *et al.* 2020 (C). Additional recalcitrance could arise from lignin condensation as lignin has been shown to self-aggregate and aggregate around hemicellulose in Kang et al 2019 (D). 18

Figure 6. The high-resolution FE-SEM images show the cellulose fibrils in the left column and sample morphology on the right for the cut stem control (A and B), stems after being milled for 2 minutes (C and D), and 15 minutes (E and F). 26

Figure 7. The cut stem control is presented in black, stems milled for 2 minutes in red, and 15 minutes in blue. The carbon 1 region of the 1500 ms 2D CP-PDSD highlights magnetization transfers between carbons 1 through 6 of each D-glucose monomer between all polymers of the cellulose fibrils in the sample (A). A 1D slice from the 1500 ms 2D CP-PDSD at 105.2 ppm in the indirect dimension is taken to demonstrate overall signal intensity change for the magnetization transfers of carbon 1 to the carbons 1 through 6 of the D-glucose monomer (B). The integrated intensity changes in the 1500 ms 2D CP-PDSD relative to the control in panels C and D have a standard deviation estimated with the noise and scaling based on the total ^{13}C content from the 30 s 1D-DP. The carbon 1-6 transfers are represented for stems milled for 2 minutes (C) and the stems milled for 15 minutes (D). 28

Figure 8. The cut stem control is presented in black, stems milled for 2 minutes in red, and 15 minutes in blue. Cellulose within the cellulose fibrils has a general atomic morphology captured by the 30 ms 2D CP-PDSD, as a more clearly outlined by the carbon 1 region (A). A 1D slice from the 30 ms 2D CP-PDSD at 105.2 ppm in the indirect dimension is taken to demonstrate overall signal intensity change for the magnetization transfers of carbon 1 to the carbons 1 through 6 of the D-glucose monomer (B). The integrated intensity changes of the 30 ms 2D CP-PDSD relative to the control in panels C and D have a standard deviation estimated with the noise and scaling based on the ^{13}C content from the 30 s 1D-DP. The carbon 1-6 transfers in red represent stems milled for 2 minutes (C) and the 15-minute milled stems (D)..... 32

Figure 9. Rigid directly bonded carbons such as those within monomers from polymers including cellulose fibrils and hemicellulose xylan substituted with arabinose and xylan are traceable carbon-carbon bonds in the 2D CP-rINADEQUATE spectrum. Integrated differences of unambiguous peaks for the cellulose carbon 4 peaks for the stems milled for 2 minutes (A) and stems milled for 15 minutes in blue (B). Subscripts i to iii are designated from most hydrated to least hydrated cellulose. In panel C the arabinose carbons 1--5 show how single quantum chemical shits on the x-axis of directly bonded atoms sum to the sample double quantum shift in the y axis, thus enabling full monomer unit to become traceable with arabinose highlighted as an example. The cellulose signal reduction apparent in the overlay control in black, stems milled for 2 minutes in red, and stems milled for 15 minutes in blue (C). Slices from the carbon 1 region of the CP-rINADEQUATE with 1D slices overlayed from the cellulose 1-2 chemical shifts has the control (black) overlayed with the stems milled for 2 minutes (red) and 15 minutes (blue)(D). Changes in structural hemicellulose peak intensities are outlined for the stem milled for 2 minutes in red (E) and 15 minutes in blue(F), both are presented relative to the control..... 35

Figure 10. Dynamic hemicellulose signals for the pectic and hemicellulose arabinose are assigned in the ^{1}H-^{13}C 2D rINEPT spectra with the carbon chemical shift on the x axis and the proton chemical shift on the y axis, with the control in black, stems milled for 2 minutes in red and stems milled for 15 minutes in blue (A). The relative signal intensity changes in the stems milled for 2 minutes in (B) and stems milled for 15 minutes in (C). 39

Figure 11. Dynamic lignin signals in the 2D rINEPT signals are outlined including lignin ether signal (A). The control is in black, stems milled for 2 minutes in red and 15 minutes in blue for the overlay (A). The initial assignment of peaks is only displayed in (A) with unambiguous signal intensities highlighted for the stems milled for 2 minutes in red (B) and stems milled for 15 minutes in blue (C). The 2D rINEPT spectra are separated in panels D--F for the control, stems milled for 2 minutes and 15 minutes, respectively. 40

Chapter 1: Introduction

Unlocking One Third of Plant biomass: Applications for the Secondary Plant Cell Wall

The breakdown of plant biomass offers a ripe opportunity to expand and replace the fossil fuel industry with crops like *Poplar volgaris* (poplar), *Panicum virgatum* (switchgrass), and *Sorghum bicolor* (sorghum) serving as appropriate sources of energy without competing with food resources.[1,2] Plant lignocellulosic biomass from the secondary plant cell wall is a sustainable and renewable feedstock for producing bio-based fuels, chemicals, and materials.[2–7] There are two types of plant cell walls: the thin and expandable primary cell wall surrounding all cells and the thicker secondary cell wall that forms as plants mature for water transport, protection, and structure(Figure 1A).[1,7–12]Due to its thickness, the secondary cell wall forms the vast majority of lignocellulosic biomass.[1] Over 90% of the secondary plant cell wall is composed of the polysaccharide cellulose, a class of polysaccharides called hemicelluloses, and the heteroaromatic polymer, lignin (Figure 1B).[1,6] These polymers can be converted via chemical or biological routes into fuels and other valuable chemicals such as hydroxymethylfurfural (HMF), benzene, and functionalized aromatics.[3,6,13–16]

Challenges Accessing the Secondary Plant Cell Wall Polymers: Insolubility and Recalcitrance

The deconstruction of the secondary plant cell wall continues to be refined as its heterogeneity and insoluble cellulose structures are challenging to study. Purification and solubilization methods are often necessary to study plant cell wall polymers.[10,17–20] In deconstruction, the inability to digest the secondary plant cell wall polymers is hallmarked by the qualitative characteristic: recalcitrance (Figure 1B). Here, recalcitrance is the inefficient breakdown and separation of secondary plant cell wall polymers in biomass.[14,21,22]

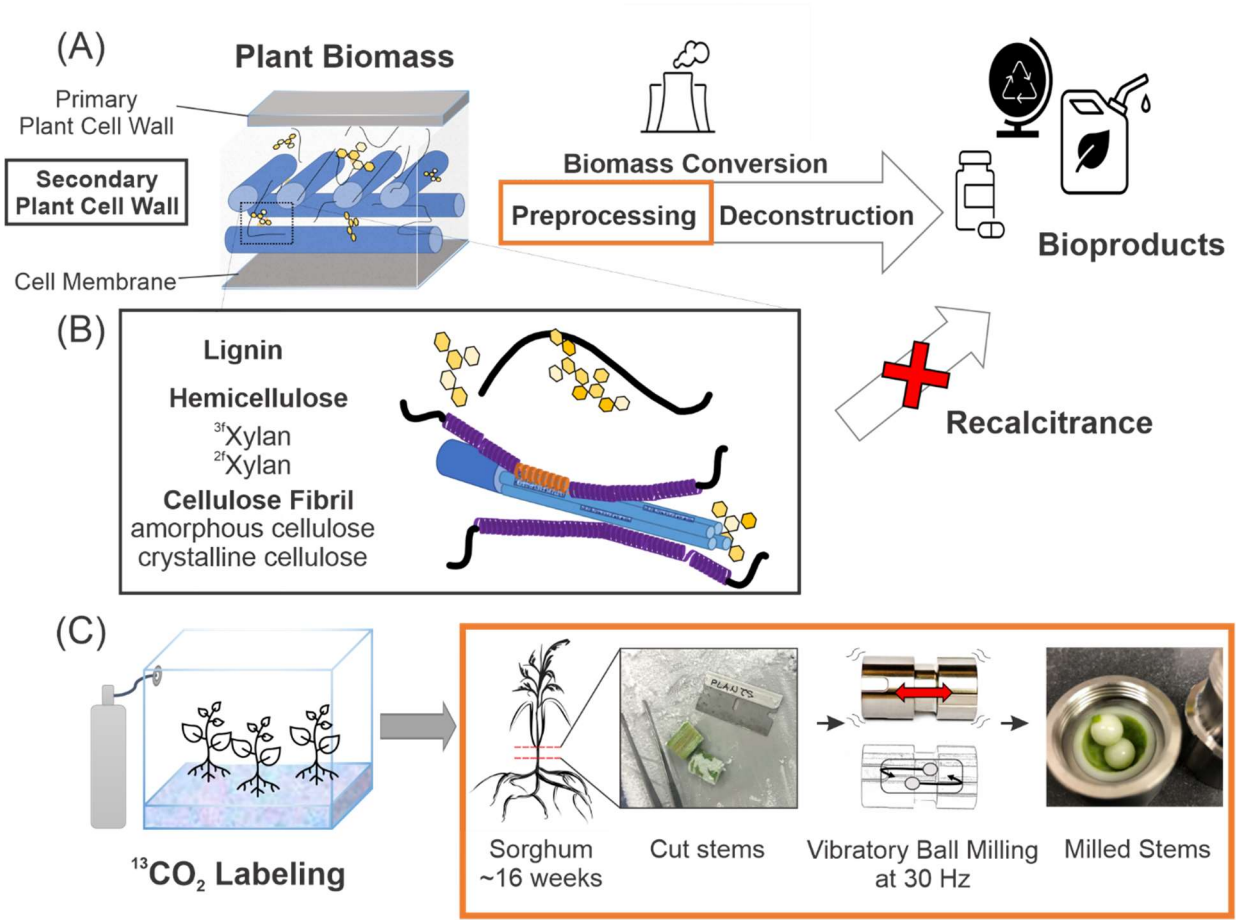

Figure 1. An introduction to secondary plant cell wall biomass conversion into bioproducts (A), structure (B), and testing for mechanically induced recalcitrance (C). Plant biomass secondary plant cell wall is highlighted and a general scheme of secondary plant cell wall conversion (preprocessing and polymer deconstruction) to bioproducts (A). A generalized diagram of the secondary plant cell wall polymers from the structural insights of previous works is outlined here,[1,23,24] and recalcitrance as an impediment to depolymerization to bioproducts[22] (B). Solid-state NMR is used to test mechanical preprocessing as a source of secondary plant cell wall recalcitrance on the lab scale with minimal additional sample manipulation (C). The advancement of $^{13}CO_2$ labeling and stem tissue enables multidimensional NMR to contrast a cut stem control with milled samples.[24–27]

Cost Effective ^{13}C Labeling Enables Structural Insight into Secondary Plant Cell Wall by Solid-state NMR

Recent advances in the incorporation of ^{13}C isotopes into living plant tissues allow characterization of the native plant cell wall structure at unprecedented resolution using solid-state Nuclear Magnetic Resonance (ssNMR).[26,28] Current efforts reveal significant diversity in the organization of plant cell wall polymers across plant species and tissue types.[23,24,28–31] Structural plant cell wall themes are highlighted in angiosperms (modern plants) for eudicot (such as Arabinose thalia and poplar) and monocots (grasses,

corn, switchgrass, and sorghum).[1,12,23–25] An updated summary of the current plant cell wall architecture is adapted from Munson *et al.* 2022 and is presented here. How multidimensional solid-state NMR contributed to plant cell wall models is central to this narrative (Figure 1B). The multidimensional solid-state NMR denotes experiments adapted from solution state NMR thanks to Magic Angle Spinning solid-state NMR (MAS ssNMR).

Without going into detail of spin Hamiltonians, MAS-ssNMR allows solid like samples to be spun in rotors at 54.7° to emulate isotropic tumbling of spins intrinsic to solution state NMR.[32] This allows for coupling of static spins in a sample due to position to be removed, namely ^{13}C-^{13}C couplings. This is important because line shapes in solid-state NMR are determined by the spin Hamiltonian which accounts for couplings, chemical shifts, relaxation(related to dynamics), and more rich information.[32,33] In particular, many Hamiltonian terms containing $(1\text{-}\cos^2\theta)$ go to zero when the sample is spun at the magic angle 54.7° but not all coupling terms are removed. High power ^1H decoupling is necessary to achieve sufficiently narrow lines in MAS-ssNMR because samples cannot be spun sufficiently fast to cancel heteronuclear couplings with ^1H.[32,34] MAS-ssNMR spectra can suffer from both homogeneous line broadening (from one spin's Hamiltonian) and heterogeneous line broadening (from multiple peaks sharing similar chemical shifts and overlapping to form one peak). NMR experiments allow for selective recoupling between spin active nuclei through bonds (J-coupling) and through space (dipolar coupling).[32,35,36] Introducing specific types of couplings, multidimensional NMR, and techniques highlighting dynamics of particular spins in pulsed techniques (NMR experiments) allow for vital detail of polymer structures in the plant cell wall.[23,24,29,31–33,37–39] In this work MAS-ssNMR is simplified and used interchangeably with solid-state NMR.

Solid-state NMR samples are packed into rotors (containers) and specific experiments can probe particular polymers allowing more native architecture of a sample to be observed. The secondary plant cell wall polymers can be probed with minimal sample preparations using solid-state NMR experiments

thanks to ^{13}C labeling (Figure 1C). Molecular changes marking recalcitrance are important to find to help refine deconstruction methods and crop engineering approaches of plant biomass conversion into bioproducts (Figure 1A). Here, mechanical preprocessing is assessed for molecular markers of recalcitrance. Sorghum stems are then used to demonstrate how solid-state NMR has the potential to assess molecular changes in the secondary plant cell wall in a bioproduct relevant crop (Figure 1C). All of this work would be impossible without cost effective ^{13}C labeling. Further discussion on how solid-state NMR to the current plant cell wall structures and relevant multidimensional solid-state NMR will be emphasized.

Chemical Composition and Organization of the Secondary Plant Cell Wall

Complexity and insolubility are major barriers for *in situ* characterization of the native plant cell wall structure.[1,40–42] The chemical composition of the secondary plant cell wall has been primarily defined as using liquid chromatography (LC),[43,44] mass spectrometry (MS),[19,45,46] solution-state NMR measurements on solvent-extracted polymers,[18,44,47] and solid-state NMR,[28,42] vibrational spectroscopy,[40] and X-ray diffraction[20] measurements on native (intact) plant tissues.

The Secondary Plant Cell Wall: Arrangement of the World's Naturally Abundant Polymers

To help the reader appreciate the potential for polymer reorganization during preprocessing, here is an overview of the current secondary plant cell wall chemical (Figure 1A) and polymer architecture (Figure 1B). In the general macroscopic organization interspersed cellulose fibrils provide an immobilized framework for a plant cell wall matrix containing water, soluble proteins, lignin, and hemicellulose polymers.[1,12] The individual cellulose fibrils are built from linear β-(1,4)-glucan polymers composed of crystalline and amorphous arrangements, which differ primarily in their water content and hydrogen bonding patterns (the precise details of which are still under investigation) (Figure 2).[48]

The cellulose fibril structure described in Figure 2 is designed by knowledge of crystalline cellulose.[49–51] So when D-glucose cellulose polymers hydrogen bonds form between polymers (without

water) and create flat crystallite sheets, a cellulose polymer is crystalline.[20,52] It is unclear whether these sheets are oriented with individual polymers with reducing ends consistently oriented;[48] to keep the structure nondescript in this continued area of study simple sheets are presented in Figure 2. Amorphous cellulose has a lower degree of order than crystalline cellulose.[53] For amorphous cellulose, hydrogen bonding may not occur strictly between cellulose polymers to form a flat sheet (Figure 2C) but may introduce hydrogen bonding between D-glucose and some water.[51,53] X-ray diffraction studies allows amorphous cellulose to be evaluated more generally as cellulose polymers creating deviations in crystallite sheets composing cellulose fibrils (Figure 2D and Figure 2E).[5,20,54] Crystallite sheets stack with Van der Waals forces to form the microfibrils contained within the larger fibril structure (Figure 2D--2G).[20,39,48,49,53,55]

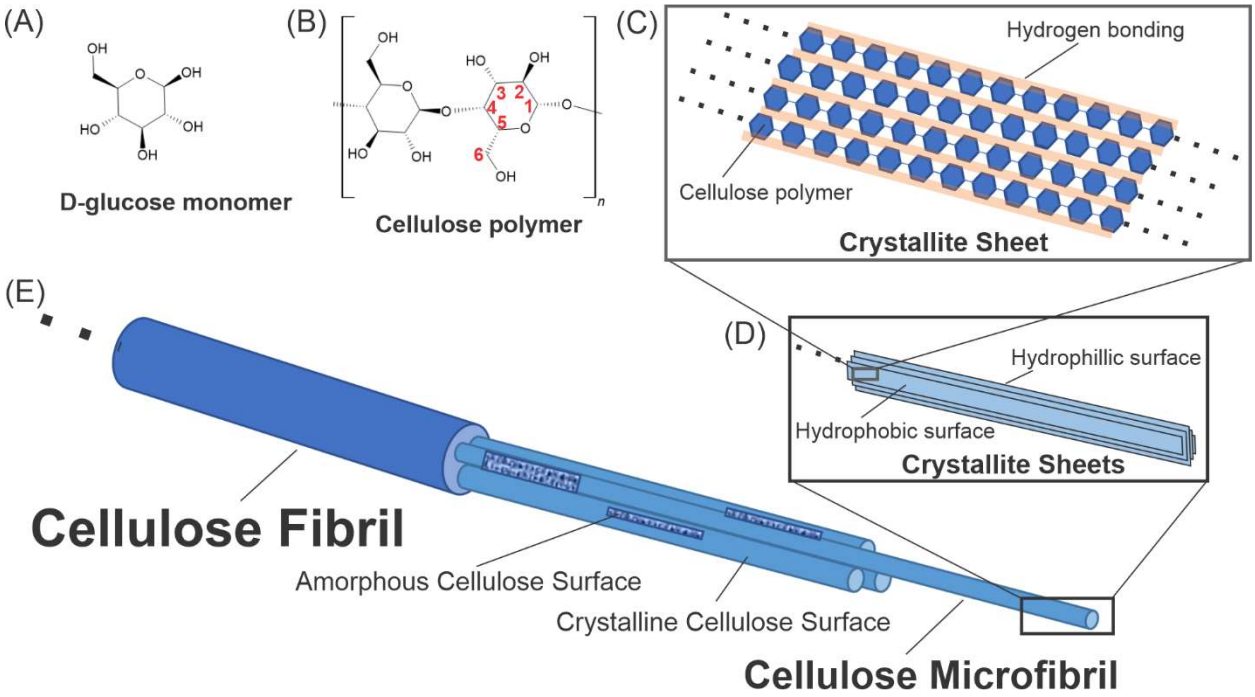

Figure 2. Work from previous literature is summarized to create a current diagram of cellulose in the secondary plant cell wall. The cellulose monomer is made of D-glucose monomers (A) and the polymer (B) is made up of β-(1,4)-glucan. Within the crystallite sheets are the individual cellulose polymer chains which hydrogen bond laterally (orange),[20,52] so when the sheets stacks together they form hydrophilic and hydrophobic surfaces (C).[1,56]Each microfibril contains crystallite sheets held together with dispersion forces from the hydrophobic faces of the sugars (D).[1,57] The cellulose fibril is composed of a collection of microfibrils (E).[1]

Hemicellulose includes 1-O-4 linear polysaccharides and pectin refers to heavily branched hemicellulose, common hemicellulose monomers are found in Figure 3A-E. Hemicellulose polymers both rigidly associate with cellulose fibrils and extend into the matrix environment where they exhibit significant molecular motion and can interact with lignin polymers in the secondary plant cell wall.[10,21,30,47] Differences across monocot and eudicot plant species have been observed, such as variable substitution patterns on hemicellulose which can dictate cellulose hemicellulose association morphology for arabinose substitutions (Figure 3G and Figure 3H).[23,24,58,59] Variable hemicellulose-lignin contacts include Van der Waals and covalent crosslinking in mature plants (Figure 3G and Figure 3F).[10,60]

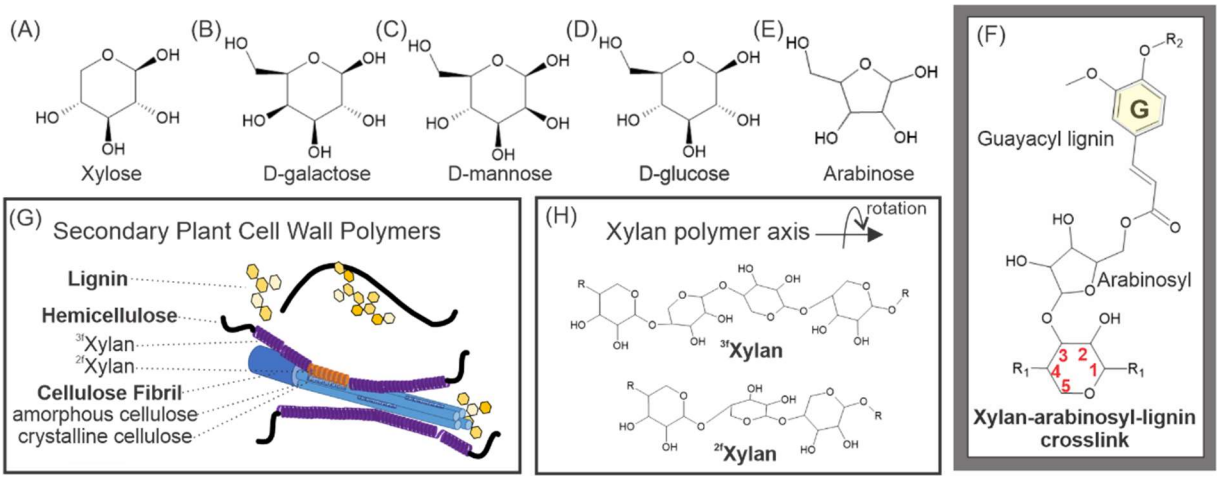

Figure 3. Structural hemicellulose monomers including xylose(A), D-galactose(B), D-mannose(C), and D-glucose(D) from polymers contain main chain linear with 1-O-4 linkages and some arabinose(E), acetylations and other decorations are excluded here and better encapsulated in Scheller and Ulvskov 2010 and Gao et al 2020. In sorghum, xylan is the prominent structural hemicellulose with irregular, prominent arabinosyl groups which can crosslink to lignin as exemplified in panel F.[10,24,60] In the secondary plant cell wall xylan hemicellulose interacts with amorphous and crystalline cellulose (G).[24] Xylan takes on a 2-fold screw axis morphology (^{2f}Xylan) along the polymer axis when it associates with crystalline cellulose surfaces (G, H).[23,24] Unbound and xylan associating to amorphous cellulose takes on a 3-fold screw axis along the polymer axis (^{3f}Xylan) (G,H).[23,24,58]

The details of lignin structure are particularly challenging to analyze due to high heterogeneity and mobility, so partial extraction of the polymer is often necessary for assessment.[3,12,42,61] Lignin is a polyphenolic network formed from the oxidative crosslinking of the monolignols p-coumaryl alcohol (H), coniferyl alcohol (G), and sinapyl alcohol (S) as well as Ferulic Acid (FA) (Figure 4A-D).[1,3,7] Lignin exists

within the plant cell matrix, interfacing with both hemicellulose and cellulose (Figure 1B).[61] Solution-state NMR in combination with MS, which relies on swelling ball-milled plant cell walls with deuterated solvents, provides detailed information on the types, functionalization, and abundance of lignin linkages present (Figure 4E).[18,19,24,44,62–65] However, due to the necessity for drying, mechanical treatment, dissolution, or solvent extraction in these techniques, previous work does not report on recalcitrance in the intact (native) secondary plant cell wall.

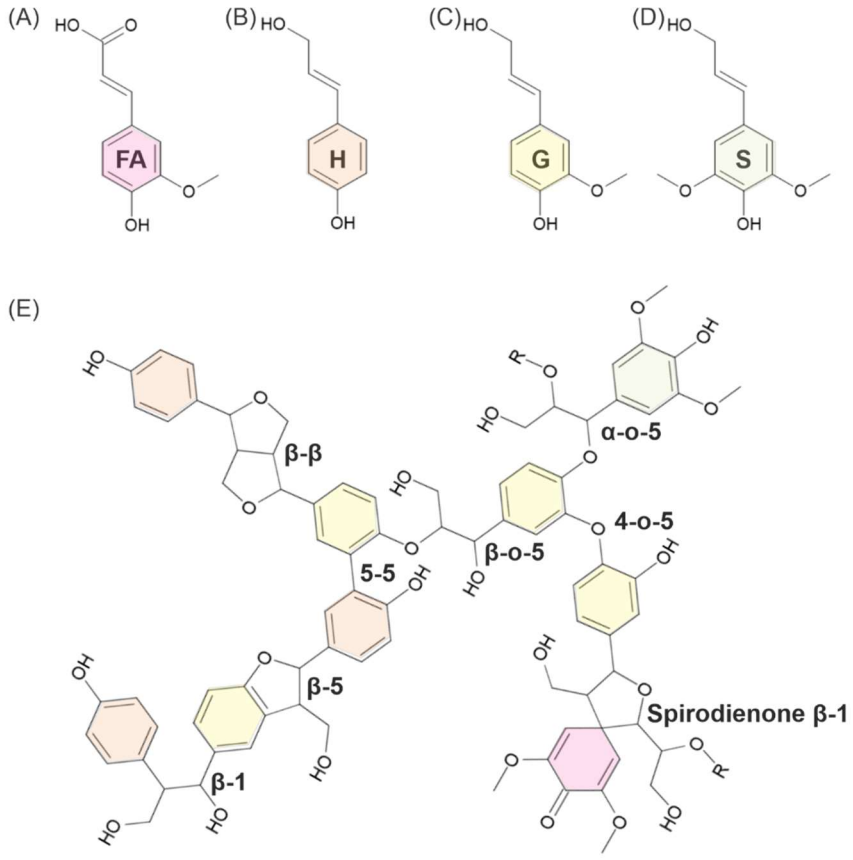

Figure 4. The heteroaromatic polymer (lignin) comprises 15-20% of the sorghum plant cell wall,[1,7,24] and is composed of monolignols and here the aromatic rings are color coded Ferulic Acid (FA) in pink(A), Hydroxyphenyl (H) in orange(B), Guaiacyl (G) in yellow(C), and Syringyl (S) in green(D). There are nine lignin linkages, only eight linkages are shown and the 4-5 linkage was excluded for simplicity (E). The β-O-4, β-5, β-β, spirodienone β-1 linkages are the most common in sorghum.[7]

Advances Toward an Accurate 3D Model for the Native Plant Cell Wall Using Solid-State NMR

Like MRI, NMR is a non-invasive way to probe the chemical environment in tissues. Unlike MRI, NMR is inherently an atomic resolution technique, as the observed signals derive from nuclear spin

magnetic moments located at precise locations in the molecules under study. In contrast to solution-state NMR, which requires solubilization of the sample, solid-state NMR methods allow for analysis of intact plant tissues. The cost of implementing solid-state NMR limited early studies of the plant cell walls. Access to cost effective ^{13}C labeling has contributed to the feasibility of understanding plant cell walls with solid-state NMR.

The requirement of NMR-active (spin active) ^{13}C isotopes was a major hurdle for characterizations of native plant cell wall structure. ^{13}C has a low natural abundance (~1%) and the cost of early efforts at isotope incorporation restricted their use. Relatively low (~11%) ^{13}C enrichment enabled early studies on hardwood.[66] The ability to detect the relative populations of rigid polymers (e.g., cellulose and a fraction of hemicellulose) was then applied to samples of pure cellulose and heterogeneous assemblies containing cellulose including paper products, cotton, wood chips, and pulp.[35,38,67–70]

While early X-ray diffraction studies demonstrated the crystalline nature of cellulose in plant cell walls,[49,50,55,71,72] solid-state NMR measurements provided more detail, such as the pattern of hydrogen bond interactions responsible for the macroscopic shape of *in situ* cellulose fibers [20,38]. A set of 1D cross polarization (CP) measurements was successfully applied to crystalline cellulose in birch and spruce biomass and offered the possibility of detecting exterior and interior cellulose components in macroscopic cellulose fibers (Figure 2E).[57,68] These straightforward 1D experiments were also useful for characterizing amorphous cellulose after ionic liquid processing of crystalline cellulose fibrils.[53] The 2D cross polarized refocused Incredible Natural Abundance Double Quantum Transfer Experiment (CP-rINADEQUATE) reports on directly bonded carbon atoms within polymers and has been useful for probing rigid structures, for example, resolving carbons 2, 3, and 5 signals of cellulose in *Populus euramericana* hardwood samples [66] and characterizing the structure of amorphous cellulose [53].

A breakthrough occurred when a highly efficient method of ^{13}C incorporation (^{13}C glucose feeding to cultured plant cells) was coupled with multi-dimensional solid-state NMR to investigate the primary plant cell wall structure.[28] This series of studies provided both a compositional and architectural description of the primary plant cell wall.[9,28,42,52,73–77] Hemicellulose-cellulose interactions were found to be much less prevalent in the primary plant cell wall than suggested by earlier models based on solvent-extracted hemicellulose and enzymatic hemicellulose digestion studies.[9,17,28,77–79] Furthermore, it was also revealed that the hemicellulose xyloglucan interacts mainly with the flat surfaces of crystalline cellulose fibers,[9,28] expanding on the idea of xyloglucan associating, crosslinking, and embedding into cellulose fibrils[69]. Semiquantitative distance measurements recorded with the Proton Driven Spin Diffusion (PDSD) experiments substantiated the organization of cellulose, xyloglucan, and pectin in primary cell walls of both monocot and eudicot cell species.[9,73,75] These advances in ^{13}C enrichment allowed the use of advanced solid-state NMR approaches shaping the primary plant cell wall architecture and how secondary plant cell wall architecture could be approached with solid-state NMR.[39]

The strategy of ^{13}C glucose feeding is not suitable to the study of the secondary plant cell wall because the plants need to be grown to relative maturity (which is prohibitively expensive) and complicated by respiration-dependent glucose synthesis (plants source carbon from the air as they mature). The development of less expensive growth chambers, utilizing ^{13}C enriched carbon dioxide as the sole carbon source, which support the growth of plants throughout their lifecycle, enabled the efficient incorporation of ^{13}C isotopes (>90%) into plant tissues.[26,27,29] Multidimensional solid-state NMR revealed significant differences in the dominant hemicellulose-cellulose contacts in different plant species.[23,24,60] For example, in eudicot Arabidopsis thaliana (Arabidopsis), 2-fold screw conformations of hemicellulose xylan (^{2f}Xn), dictated by even patterns of substitutions, enable a close association with crystalline cellulose (Figure 1B).[23,58] In contrast, in monocot sorghum, the high degree and irregularity of arabinose substitution patterns on xylan dictate a 3-fold screw conformation (^{3f,A}Xylan), enabling

association with amorphous cellulose (Figure 3C).[24] Additionally, in softwoods, cellulose fibrils can be tethered by both xylan and mannan hemicellulose, increasing the strength of the plant cell wall.[31] For the sorghum case, limitations in biochemical techniques prevent the analysis of carbohydrate substitutions on xylan and the solid-state NMR measurements which can show the xylan-cellulose interaction that is otherwise unobtainable using other methods (Figure 4C).[24]

Carbon dioxide ^{13}C labeling and new applications of advanced solid-state NMR techniques have helped elucidate the structure of lignin in the secondary plant cell wall. Signal enhancement by dynamic nuclear polarization (DNP) demonstrated that lignin directly bridges hemicellulose polymers and interacts strongly with cellulose fibers in uniformly labeled switchgrass, highlighting the role of lignin in supporting the 3D organization of hemicellulose and cellulose.[30] However, effective penetration of the DNP reagent into the plant cell wall for this signal enhancement required 15–20 min of milling,[30] which could perturb native lignin structure. Direct polarization (DP) experiments utilizing PDSD performed on ^{13}C enriched poplar stems highlight a potential avenue to probe lignin contacts and spatial proximities through selective excitation and magnetization transfer from lignin to other polymers,[80] which provide support for the putative organization of lignin in poplar,[81] switchgrass,[30] and Arabidopsis[29]. Further development of selective excitation and other solid-state NMR methods to probe biomass with minimal sample manipulation have the potential to provide a more complete picture of the secondary plant cell wall structure and how established sample preparation methods influence that structure.

Although a wide variety of solid-state NMR methods can be applied to highly ^{13}C enriched plant tissues, two methods provide rapid and straightforward characterization of the polymer organization in the secondary plant cell wall. First, the INADEQUATE approach provides an avenue for the characterization of the polymers present within a secondary cell wall sample at relatively high resolution and can distinguish at least three populations of amorphous and crystalline cellulose, in addition to three populations of xylan.[23,24] Second, ^{13}C-^{13}C recoupling methods, such as PDSD and Dipolar Assisted

Rotational Resonance (DARR), report on the spatial proximity of cellulose, hemicellulose, and lignin.[23,24,30,31,58] Polymers free, dynamic, and in the plant cell matrix are captured by the refocused Incredible Nuclear Enhancement by Polarization Transfer (rINEPT) experiment.[32,34] Lower power proton decoupling is used in the rINEPT so polymers only with high intrinsic mobility (such as free polymers) are detectable.[32] The rINEPT experiment techniques share commonalities with solution state NMR experiments used to evaluate lignin content in deconstruction efforts and marks an upper limit of dynamic polymers which can be captured with solid-state NMR.[6,7,82] These experiments provide a more complete picture of the polymers in the plant cell wall than has ever been obtainable before.

Chapter 2: Studying Mechanically Induced Recalcitrance

Recalcitrance of the Secondary Plant Cell Wall Proposed from Mechanical Preprocessing

At first glance, the recalcitrance of the secondary plant cell wall would seem to be inherent to the material as it can arise from the dominant polymers of the structure targeted in deconstruction.[1]

In plants, cellulose fibrils have genetically and environmentally determined sizes so continuous fibrils change their direction and length resulting in nonuniform fibril orientations in plant tissues.[11,48,51,57] Amorphous cellulose is important in the plant cell wall because they support cellulose fibril junctions so fibrils can change directions and adapt in tissues.[1,11,24,48,51,57] For plant cellulose fibrils (Figure 2), only a fraction of the cellulose polymers have perfect hydrogen bonding patterns and order associated with crystalline cellulose.[48,51] Crystalline cellulose is predicted to be more digestible in deconstruction by hydrolases for chemicals like HMF.[13,56,83] Amorphous cellulose polymers in plant cellulose fibrils are associated with indigestible material and treated as a marker for recalcitrance.[5,83,84] However there is still ambiguity regarding if the amorphous cellulose is recalcitrant due to being out of register cellulose within the polymer assembly (Figure 2).[48,51,53,56,67] Considering enzyme digestion, the current consensus correlates the amorphous cellulose content within fibrils with recalcitrance,[83,84] which can be correlated with a crystallinity index[54].

Hemicellulose, the 1-O-4 linked linear polysaccharides contributing to the structural strength of the plant cell wall, interacts with both lignin and cellulose.[1,10,23,24,30,58,80] The role of hemicellulose as a tethering component within the plant cell wall was first proposed in the primary plant cell wall structure[17,78,79] and coheres with mechanical strength of plants provided by the secondary plant cell wall.[23,24,31,58] Past deconstruction methods targeting hemicellulose resulted in higher recalcitrance.[22,85] Even with ionic liquid digestion, early NMR studies with pulsed sequences show decreased lignin yields and increase in amorphous cellulose.[44]

Structural hemicellulose associating with amorphous cellulose fibril surfaces concerns recalcitrance when more amorphous cellulose surfaces form upon mechanical processing as predicted by milled cellulose fibrils in cotton.[5,24] Structural hemicellulose also crosslinks with lignin upon plant maturity [10,60] which greatly complicates digestion of roughly 60% of the secondary plant cell wall. In fact, hemicellulose-first deconstruction methods were largely abandoned due to high observed recalcitrance and supported the switch for deconstruction techniques to focus on lignin first extraction from the secondary plant cell wall (and biomass materials).[3,86]

Finally, lignin is critical to the plant and plant development within all species,[1,7,81] and high lignin content is associated with recalcitrance[21,22]. High ratio of G/S lignin is attributed to greater heterogeneity and branching patterns within lignin networks and thus correlated with recalcitrance (Figure 3C).[46,82,87] Past correlations of recalcitrance outputs to the order in which polymers are digested have directed many deconstruction techniques to a “lignin first” model.[21,86] Unfortunately, lignin also plays a vital role in plant water transport, pathogenic protection, and maturity; many mutations aimed at eliminating lignin are lethal to the organism.[1,8,87]

Advancements in Overcoming Plant Cell Wall Recalcitrance

The high recalcitrance of the secondary plant cell wall is a major bottleneck in the extraction of chemical precursors from lignocellulosic biomass in the deconstruction pathway.[1,22] Strategies to decrease

this intrinsic recalcitrance include the development of plants with altered biomass composition[88] and novel deconstruction methods, such as the use of new solvents [89] and enzyme cocktails which target key polymer linkages [90]. However, deconstruction methods can also introduce recalcitrance, for example by the deposition of more condensed lignin following solubilization.[21] The formation of new molecular contacts defining recalcitrance are challenging to assess in biomass[22] and continue to be under investigation. [1,16,60]

Recalcitrance Reintroduced During Deconstruction Techniques of Biomass

The complexity and insolubility of plant cell wall samples often requires heavy sample manipulation in deconstruction.[1,10,12,91] However, whether recalcitrance is introduced in sample preparation of plant biomass conversion to bioproducts is a complicated issue to address given the major discrepancies between lab and industrial processes. [2,14,22] An immediate motivation to adopt more systematic approaches is the energy investments differing between the lab and industrial scale.[2,14,92] This can become problematic in cases involving massive solvent extraction techniques and other preprocessing techniques as energy does not always scale from laboratorial to industrial settings. One example is the frequently used mechanical preprocessing at the lab scale which often proves to be too energetically expensive at the industrial scale.[92] So, tracking assumptions and changes in the native plant cell wall structure behind the discrepancies is critical so that lab scale optimizations can benefit industrial applications.

Mechanical preprocessing is commonly used to reduce biomass particle size to increase solvent accessibility and polymer solubilization.[93,94] Lab scale vibratory ball-milling achieves this goal by rapidly vibrating a chamber containing lignocellulosic biomass with grinding balls (Figure 1C). Importantly, past studies on the plant cell wall structure used mechanical milling to prepare samples for analysis,[18,30] so the outcomes have been influenced by non-native interactions and contacts between these polymers.[3,61,83,93] However, milling leading to recalcitrance is frequently reported during lignocellulosic biomass conversion

efforts, impeding the efficiency of subsequent processing and separation steps.[21,61,95] Common preprocessing sample preparations taken before specific deconstruction methods should be under investigation because of the potential for introducing wide spread recalcitrance.

Tracking Mechanically Induced Recalcitrance

Mechanical preprocessing leading to recalcitrance is reported during lignocellulosic deconstruction pathways at the lab scale, which impedes the efficiency of subsequent steps in biomass processing.[21,87] Milling induced recalcitrance could be due to the production of reactive lignin species[93] promoting aberrant hemicellulose-lignin crosslinks[60] as the lignin self-associates and condenses,[21,30] resulting in polymers which may be less accessible for digestion (Figure 5A). Additionally, increased amorphous cellulose content and exposed cellulose surfaces produced from milling cellulose fibrils[5] could induce reorganization of hemicellulose-cellulose contacts due to their multiple modes of interaction in the native plant cell wall[23,24]. Although the cost of applying milling to biomass as a technique on an industrial scale makes it energetically impractical to apply, the impact of potential recalcitrance induction during lab scale methods development could still influence efforts in developing deconstruction pathways and estimating their effectiveness.

One recent study on milling cellulose fibrils offers potential insight into what happens to cellulose fibrils.[5] Cellulose fibrils are nonuniformly oriented in the plant cell wall which results in irregular signal detection making some spectroscopic techniques challenging on intact material. [5,11,96] Cellulose fibrils scatter light nonlinearly because crystalline cellulose belongs to a noncentrosymmetric crystal group (P_{2_1}).[20,38,55,71] Milling pure cellulose in cotton allowed for easier sample orientation which is important in the Ling et al. 2019 study contrasting 13 different techniques to study crystallinity, including x-ray scattering techniques, vibrational spectroscopy and 1D CP solid-state NMR. In the study, Field-Emission Scanning Electron Microscopy (FE-SEM) was used to monitor sample morphology for cotton milled between 15--120 minutes at 30 Hz. The original proportion of amorphous and crystalline cellulose before

and after milling and 30--50% of sample crystallinity was lost after milling cotton for 15 minutes. Based on 1D CP solid state NMR measurements around 40% of crystallinity was lost and the initial crystallinity of the sample accounted for some inherent amorphous cellulose compared to x-ray scattering techniques. When pure cotton cellulose was milled crystalline cellulose fibrils showed loss in crystallinity and a consistent increase in amorphous cellulose, supporting mechanical preprocessing could induce recalcitrance.

To test the current mechanical induced recalcitrance hypothesis in mechanical preprocessing, sorghum stems were subjected to lab scale vibratory ball-milling. In this study, stem tissue was used for initial experiments to allow for the highest concentration of secondary plant cell wall to increase the likelihood of observing recalcitrance with the greatest signal-to-noise ratio possible for solid-state NMR. Monitoring changes in sample morphology of the cellulose fibrils by FE-SEM is necessary because milling times vary depending on the biomass, sample quantity, and desired particle size.[3,5,18] The time points include milling for 2 minutes at 30 Hz as common initial mechanical preprocessing time consistently executed for biomass[18] and 15 minutes of milling at the same frequency to emulate longer milling times. Contrasting the effects of milling pure cellulose and milling cellulose in the plant cell wall also informed the selection of the 15-minute milling time point.

Molecular changes in secondary plant cell wall polymers are probed with an initial set of solid-state NMR experiments. The rINEPT was expected to selectively probe the highly dynamic (free and solvated) polymers, lignin, and hemicellulose. The CP-rINADEQUATE [66] probes directly bonded carbons in rigid components such as cellulose of the cellulose fibril and hemicellulose associated to cellulose fibrils. The CP-PDSD experiments were used to monitor the atomic cellulose morphologies using through space carbon-carbon correlations. Molecular recalcitrance markers include mobility and contacts of the dominant polymers by solid-state NMR experiments for polymers lignin, hemicellulose, and cellulose.

Markers of Recalcitrance Hypothesized for Ball-milling from Literature

Monitoring markers of recalcitrance can be subdivided into each type of polymer. During the milling process crystalline cellulose is expected to convert to amorphous cellulose according to previous work on pure cellulose fibril structures of cotton by 1D NMR, FE-SEM, and vibrational spectroscopy.[5] The resulting conformation change to amorphous cellulose within the plant cell wall may result in decreased access to crystalline planes of cellulose necessary for enzyme digestion (Figure 5B).[7,47,95,97] Assuming sample matter is conserved and no digestion occurs, proportions of crystalline and amorphous cellulose content in cellulose fibrils can be reported by NMR.[5] Unlike vibrational spectroscopy where there is high signal overlap and sample crystallinity indexes afforded by x-ray diffraction, NMR contains well separated signatures for amorphous and crystalline cellulose (Table S1). Cellulose polymers on the dehydrated interior, center, and more hydrated interior cellulose polymers of the cellulose fibril have distinguished chemical shifts over the last 20 years of experiments and specifically identified for sorghum (Table S1).[24]

In 2D solid-state NMR experiments plant cell wall polymers compromise over a third of biomass and most of the signals due to the ^{13}C labeling technique. When examining the plant cell wall in the spectra the carbon neutral region of polysaccharides and lignin is 120--60 ppm and 170--110 ppm, respectively.[23,24,95] Tracking proportional intensity changes of amorphous and crystalline cellulose distinguished by their chemical environments is possible. Cross Polarized (CP) NMR experiments will select for the rigid polymers as the experiments are able to spectroscopically separate the rigid portions of the plant cell wall including the cellulose fibrils. CP based solid-state NMR experiments are more efficient for spins stagnant in space (rigid) polymers of the plant cell wall. Cellulose fibrils are solid structures which can be probed with CP based solid-state NMR.

Hemicellulose rigidly associated to cellulose in cellulose-hemicellulose interactions would also be selected for using CP experiments (Figure 5C).[23,24,58] In the context of the plant cell wall, cellulose-hemicellulose interactions do vary based on the morphology of cellulose,[23,24] so recalcitrance could also

occur by additional amorphous cellulose-hemicellulose interactions common in grasses such as sorghum.[24] Hemicellulose signals would then increase in their rigid signal intensity according to CP experiments and decrease in signal intensity from the highly dynamic signals.

The highly dynamic signals captured in the rINEPT include ^{1}H-^{13}C correlations in the 2-D experiment and lignin with the plant cell wall. Lignin reorganization could cause recalcitrance in a variety of ways. One observable way would be cross-linkages forming due to mechanical activation lignin-arabinose-xylan (additional cross-linkages between lignin and hemicellulose) (Figure 3B, Figure 5C). The ether signals within lignin branching and lignin-hemicellulose cross-linkages are captured within the rINEPT experiment.[34,60] Lignin condensation, aggregation, and crosslinking noted in recalcitrance means highly dynamic lignin content is lowered (Figure 5C and Figure 5D), resulting in an expected decrease in signal intensity in the rINEPT. Digestible hemicellulose and cellulose would be reduced as polysaccharides are trapped as lignin condenses in the secondary plant cell wall (Figure 5D).

Based on previous ^{13}C evident methods and solid-state NMR analysis, the molecular evaluation of secondary plant cell wall architecture is feasible for bioproduct relevant crops such as sorghum.[6,24] This research project aims to identify where recalcitrance occurs in the deconstruction pathway and identify markers of recalcitrance using 2D solid-state NMR. The first step of the deconstruction pathway (mechanical preprocessing) is investigated for mechanically induced recalcitrance for ^{13}C labeled sorghum.

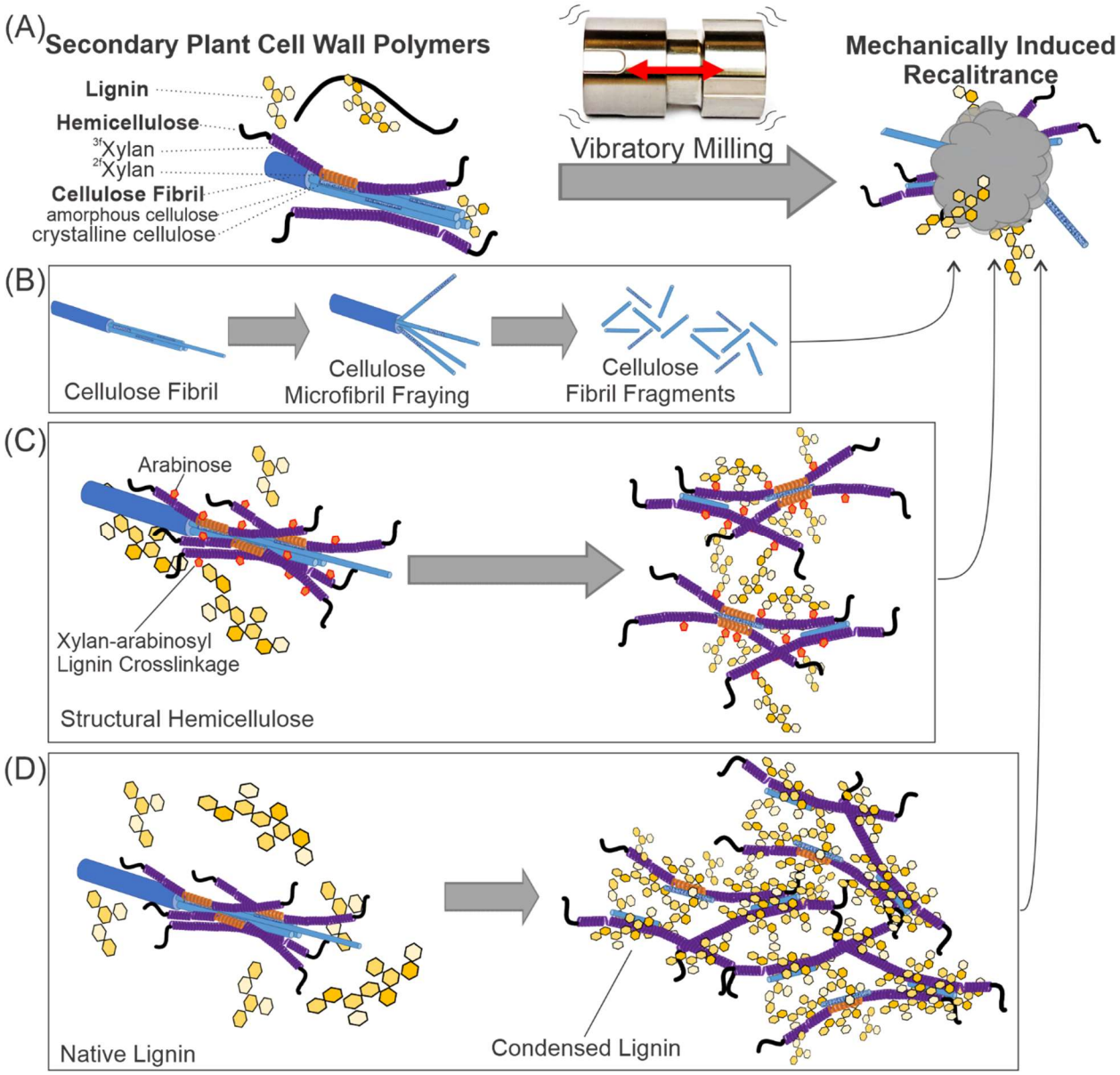

Figure 5. The proposed mechanical induced recalcitrance scheme in panel A can be broken down by recalcitrance from each polymer. These original schemes summarize findings from previous literature. Cellulose conversion from crystalline to amorphous cellulose is a reported source of recalcitrance (B).[5,54,84] Structural hemicellulose further associating with cellulose surfaces or increasing cross-linkages between xylan and lignin noted in Terrett and Dupree 2019 and given ^{3f,A}Xylan and ^{3f}Xylan both associate with amorphous cellulose in sorghum as discovered in Gao *et al.* 2020 (C). Additional recalcitrance could arise from lignin condensation as lignin has been shown to self-aggregate and aggregate around hemicellulose in Kang et al 2019 (D).

Evaluation of Recalcitrance Markers in 2D Solid-state NMR Experiments: Chemical Shifts and Integration

How the heterogeneous secondary plant cell wall changes from preprocessing needs to be carefully approached. This work primarily focuses on intensity changes of unambiguous signals within the

established sorghum native plant cell wall (before and after milling) to circumvent misassignment of polysaccharide non-ambiguous peak changes which shift to ambiguous, overlapped chemical shifts during deconstruction. Gao et al. 2020 is used as a reference for secondary plant cell wall polymer chemical shift assignments confirmed in sorghum from previous literature which relied on extracted polymers,[7,18,38,53,67,68] computational verification,[23,24] and previous solid-state NMR[9,23,28–31,39] on the architecture of the plant cell walls.

Additional structural information can be confirmed from chemical shifts using computation, allowing for polymer morphological changes to be assessed based on changes in monomer orientation.[23,29,33,80] Future work using data collected in this work could offer greater insight into polymer morphology changes. Given the heterogeneity of the plant cell wall samples, examining the recalcitrant markers would narrow the relevant chemical shift and chemical shift changes by computation as well as contrast chemical shifts of extracted polymers.

Chemical shifts can support changes in polymer enviornments when peaks are well dispersed and unambiguous within a 0.5 ppm (Table S1). For example, accessible polymers are expected to be more hydrated and have chemical shifts downfield (i.e. digestible hemicellulose and cellulose fibril surfaces). As cellulose fibrils are broken down into more disperse microfibrils or cellulose substructures, as discussed in Figure 2C, the chemical shifts of amorphous and crystalline cellulose may be expected to move downfield (Figure 5B). Additional hemicellulose-cellulose association on hydrophilic surfaces of cellulose polymers would have chemical shifts potentially shift upfield for both polysaccharides (Figure 5C). Upon the hemicellulose crosslinking to lignin may also result in chemical shift changes downfield for hemicellulose due to deshielding from bonding with the conjugated heteroaromatic lignin (Figure 5C). However, recalcitrant organization of lignin trapping hemicellulose and cellulose in self-aggregation (Figure 5D) would reduce surface water may have chemical shifts moderately upfield compared to the expected literature values in sorghum based on Gao et al. 2020 assignments of the secondary plant cell wall. These

are generally anticipated chemical shift changes in polymers which is somewhat challenging given signal overlap of polysaccharides. In this work changes in chemical shift after mechanical preprocessing are highlighted by 2D integration of chemical shifts found in the control (native plant cell wall). Integration allows for minor changes or gradual changes in the plant cell wall to be assessed, increasing the ease of interpreting reasonable chemical shift changes upon preprocessing (assuming no matter is lost).

Chapter 3: Methods

Growth of the ^{13}C Labeled Plant Material

Sorghum (*Sorghum bicolor* variant Tx430) was grown hydroponically and then transferred to a growth chamber for carbon dioxide ^{13}C labeling until they reached 16 weeks by collaborators Yu Gao and Jenny Mortimer as described in Gao *et al.* 2020. The sorghum was incorporated with 92% ^{13}C according to elemental analysis and are physiologically normal organisms.[24] Upon harvest, the plants were flash frozen in liquid nitrogen, divided by tissue type (roots, leaves, and stems), and cryogenically stored for later studies. Samples were transported on dry ice between labs and stored at −80 °C for the duration of the study.

Sample Preparation of Sorghum Stems

The bottom third of sorghum stems sourced from collaborators were utilized as standard conditions of the secondary plant cell wall within the mature "stem tissue" of the plant per their previous procedure.[24] Sorghum stems were all cut at approximately −20 °C over dry ice on a steel cutting surface into 1--2 mm^2 pieces. The control was cut sorghum stems weighing approximately 400 mg. For milled samples, 600 mg of cut sorghum stems were prepared. Cut stems were stored in the −80 °C freezer for later use.

Milling Conditions of Plant Materials

Cut stems were milled using a Retch MM400 in a 10 mL zirconium grinding jar with two 10 mm zirconium beads at 30 Hz. For the 2-minute milling timepoint, 600 mg of cut stems were milled for a single

2-minute interval. For the 15 minute milling period, 600 mg of cut stems were milled in cycles for 5 minutes followed by 5 minute resting periods in accordance to relevant lab scale milling procedures from previous literature.[5,18] After the milling period, the samples were divided into several cryogen vials and flash frozen in liquid nitrogen before storage in the −80 °C freezer.

Sample Morphology Tracked with FE-SEM

FE-SEM was employed to check sample morphology, specifically cellulose fibril morphology structures after milling. A Hitachi S-4100 T Scanning Electron Microscope was used to collect high resolution images for the control and milled samples using a procedure detailed in Zheng *et al.* 2020.[98] A 10 nm gold coating was sputter coated onto control and milled sorghum samples with a Cressington 208hr Sputter Coater. FE-SEM images were collected at a working distance of 15–6 mm with acceleration voltages ranging from 2–10 kV to achieve optimal spectra resolution.

Atomic Resolution of Sorghum Stem Secondary Plant Cell Wall by MAS-ssNMR

NMR experiments were performed on a Bruker 500 Solids NMR Spectrometer (11.7 T magnet), with a Bruker 4 mm MAS probe and at a MAS speed of 10 kHz at the UC Davis NMR Facility. All samples were shimmed using a water sample file on the instrument. Two channels were utilized on the 500 MHz instrument, one was set to SFO2 500.0305 MHz for the proton and the other was set to 125.7445782 MHz for ^{13}C. Spinal 64 ^{1}H decoupling was used.[32] A 20% CP ramp was applied on the ^{13}C to increase the efficiency of transfer. Decoupling powers were optimized for ^{1}H radiofrequencies of 71 kHz. The radiofrequency(RF) power for CP on the carbon for the 1D and 2D NMR was a matched between protons and carbons at the 10 kHz MAS spinning frequency.[32] Optimization of the ^{1}H and ^{13}C RF pulse lengths for each sample were obtained by locating nulls a carbonyl signal around 100 ppm in a 1D CP experiment with 4 scans with parameters similar to the 1D CP in Table 1. An 1-^{13}C L-alanine sample was used to check instrumentation and calibrate chemical shifts on the TMS scale using a 1D CP experiment prior to data collection on the plant samples.[99] Beyond these commonalities, parameters for the experiments applied to all the control

and milled samples are summarized in Table 1. Samples were packed into 4 mm zirconium rotors with two 2 mm Teflon discs cut from Teflon tubing on the top and bottom to center the ^{13}C sample. All data collection occurred at room temperature. Experiments on control stems revealed the total time of sample viability in the spectrometer to be approximately 52 hours and this was tracked for all experiments by periodic the collection of 1D CP and DP spectra for all sample data collections (Figure S1). The 2D was collection is divided into two sets of experiment collection per experiment as summarized in Table 1 and added together in NMRpipe for processing. NMR data were processed in NMRpipe with Gaussian line-broadening applied before the Fourier Transform.[100] Spectra were plotted in Sparky[101] and formatted in Corel Draw 2019.

A quantitative 1D DP experiment was employed to properly scale data on the milled and control samples for integration. Parameters of the quantitative 30 s 1D DP experiments were like 1D-DP experiment in Table 1 but the recycle delay was adjusted to 30 second recycle delay to assess the ^{13}C content within the control and the milled stem samples.[24] After data collection samples were stored at −80 °C in their respective 4 mm rotors for later use in the 1D-DP to quantitatively scale the sample loading of the samples which varied in consistency (Figure S2). The 30 s 1D-DP allowed for integrations across all experiments for each sample to be scaled for sample load which varied due to the consistency variation in the cut and milled samples (Figure 2C).

Milled samples were flash frozen before NMR data collection without changes to the plant cell wall. Cut stems were thawed for 3.5 hours based on the appropriate milling time for DMSO gel swelled plant cell walls of grasses outlined for 600 mg of material in Kim and Ralph 2010. Experiments in Table 1 and a DP-rINADEQUATE show no detected changes (Figure S3). The DP-rINADEQUATE had the same experimental parameters outlined in the CP-rINADEQUATE summarized in Table 1 with the cross polarization removed and the ^{13}C nuclei directly irradiated (dpRINADEQUATE.crm). This meant samples could be milled, flash froze, and rethawed for data collection.

Table 1: Experiment parameters for MAS-ssNMR on the 500 MHz Bruker Instrument. All experiments were performed on a 4 mm Bruker probe in a 500 MHz Bruker magnet at a 10 kHz spinning speed at room temperature. The number of scans for the experiment (NS), FID points (TD), the FID acquisition time (AQ), dwell time (DW), pre-scan delay is (DE), and recycle delay (D1) are specified. The CP contact time between protons and ^{13}C is listed ($CP_{H\text{-}13C}$). The 100 kHz Sweep width (SWH) and receiver gain (RG) at 1820 Hz was kept consistent kept consistent in the direct dimension measurements and 1D measurements. For 2D experiments, the indirect sweep width (SWH_{ind}) and the FID parameters varied with each experiment. Indirect FID points(TD), acquisition time (AQ), increment for delay between FID points (D_{FID}), and resolution (RES_{FID}). The experiment script file and FID mode(far right) are listed.

Experiment	Parameters	Program and FID mode
1D-DP	NS=128 DW=5.00µs DE=10.00µs D1=2s RG=1820Hz SWH_{dir}= 100kHz TD_{dir} =1536 AQ_{dir} =7.7350ms RES_{FID}= 65.104Hz	hpdec.av qsim mode
1D-CP	NS=128 DW=5µs DE=10µs D1=1.5s RG=1820Hz $CP_{H\text{-}13C}$=1ms SWH_{dir}= 100kHz TD_{dir} =1536 AQ_{dir} =7.7350ms RES_{FID}= 65.104Hz	cp90.crm qsim mode
2D CP-rINADEQUATE	NS=64 DW=5µs DE=10µs D1=1.5s RG=1820Hz $CP_{H\text{-}13C}$=1ms SWH_{dir}=100kHz TD_{dir}=1536 AQ_{dir}=7.7350ms RES_{FIDdir}= 65.104Hz SWH_{ind}=47619.047Hz TD_{ind}=250 IN_F=21µs AQ_{ind}=2.625ms RES_{FIDind}=190.476Hz	cpRINADEQUATE.crm qsim
2D CP-PDSD 30ms	NS=16 DW=5µs DE=10µs D1=1.5s RG=1820Hz $CP_{H\text{-}13C}$=1ms $CP_{13C\ Mix}$=30ms SWH_{dir} = 100kHz TD=1536 AQ_{dir} =7.735ms RES_{FIDdir}= 65.104Hz SWH_{ind}= 35714.285Hz TD=370 IN_F =28µ AQ_{ind} =5.18ms RES_{FIDind}=96.525Hz	cpdarr.dm States-TPPI
2D CP-PDSD 1500ms	NS=16 DW=5µs DE=10µs D1=1.5s RG=1820Hz $CP_{H\text{-}13C}$=1ms $CP_{13C\ Mix}$=1500ms SWH_{dir} = 100kHz TD=1536 AQ_{dir} =7.735ms RES_{FIDdir}= 65.104Hz SWH_{ind}= 35714.285Hz TD=370 IN_F =28µ AQ_{ind} =5.18ms RES_{FIDind}=96.525Hz	cpdarr.dm States-TPPI
2D rINEPT	NS=16 DW=5.00µs DE=10.00µs D1=1.5s RG=1820Hz SWH_{dir} = 100kHz TD=1536 AQ_{dir} =7.7350ms RES_{FIDdir}= 65.104Hz SWH_{ind}=1333.333Hz TD=334 IN_F =75µs AQ_{ind} =12.525ms RES_{FIDind} =39.9202Hz	rinept.crm qsim mode CP waltz

Chapter 4: Results and Discussion

Monitoring Secondary Plant Cell Wall Reorganization During Ball-Milling

Examining the reorganization of the secondary plant cell wall polymers due to mechanical preprocessing is important for the development of the plant cell wall model and effective utilization of biomass without recalcitrance.[1,22,42,102] Conversion from plant biomass to bioproduct often necessitates mechanical preprocessing in deconstruction methods; milling times vary but can be as short as 2 min and can exceed 4 hours.[97,103–105] Milling of stem tissue at 30 Hz for 2 min was selected to allow direct comparison to DMSO swelling studies employing the same milling time.[18] Typically plant cell wall samples are milled at 30 Hz for 2 minutes at 30 Hz followed by up to 24 hours of milling at 10 Hz depending on the amount of material.[18] As a result, these experiments report on cell wall structure after reorganization of the plant cell wall polymers that occur during mechanical preprocessing. For example, solid-state NMR measurements on maize biomass after mechanical and solvent processing methods support lignin association with the surface of hemicellulose coated cellulose fibers in the cell wall,[61] a different result than those obtained from recent solid-state NMR measurements on less processed grass and other plant species biomass.[24,30,31] $^{13}CO_2$ labeling is challenging for large mature plants such as Poplar trees given labeling chambers would need to adapt over the lifecycle of the organism, and there are few commercial sources.[24,26,30,80]

In this current study, the results of mechanical processing on ^{13}C sorghum data collected at common laboratory milling times are available for native and milled stems to contrast the tissue with the highest amount of secondary plant cell wall to boost sensitivity solid-state NMR recalcitrance markers. Comparisons are limited to changes in signal intensity signal through the integrated comparison of peaks found in the control to the milled samples for the CP-PDSD experiment, CP-rINADEQUATE, and the rINEPT (Table S1). Polymers are evaluated across the secondary plant cell wall structure by combining the CP based experimental observations which examine highly rigid components and the rINEPT highly dynamic components of the sample. This current work also highlights initial characterization of highly dynamic

lignin and hemicellulose polymers of the plant cell wall matrix in the rINEPT for the first time (Figure 11, Figure S4, and Table S2-4). However, the sorghum stems milled for 15 minutes will be compared to previous work by Ling *et al.* 2019 which shows that cotton crystallinity of cellulose decreases by an average of 40% over 13 techniques.[5] This is important because cotton is a naturally pure form of cellulose (~92% comprised of cellulose fibrils)[5,38] and results from milling cellulose in the secondary plant cell wall can be observed in the sorghum stems milled for 15 minutes. For simplicity, the results are ordered by polymer class presented in Figure 2B: cellulose fibrils, structural hemicellulose, and lignin.

Cellulose Fibril Changes During Milling

Cellulose Fibril Morphological Changes

FE-SEM images of the control and milled samples in Figure 6 show the morphological structure of the cellulose fibrils in their bundled cylindrical form as lines. Cellulose fibrils are typically on the order of 1-2 µm in diameters for a scale reference,[48] which is on the order of some milling efforts of softwood "fines".[94] In Figure 6A the cellulose fibrils are shown in their bundled structure to the right in Figure 6B of the stem vasculature which can be seen as the large main cylindrical shape with thin cellulose fibrils forming lines across. After milling, the vascular structures comprising the stem are lost (Figure 6D and Figure 6F), this makes sense as the macroscopic stem structure is homogenized into a paste upon milling (Figure 2C).

However, the cellulose fibril structure remains after 2 minutes and 15 minutes of milling (Figure 6C, Figure 6E). Contrasting the control and stems milled for 2 minutes at 30 Hz, the individual cellulose fibers within the sample are largely similar, with a slightly rougher texture (Figure 6C). After 15 minutes of milling stems at 30 Hz, there is noticeable fraying of the cellulose fibril bundles within Figure 6E, the thinner cylindrical lines appear to be consistent with microfibrils (Figure 2E).

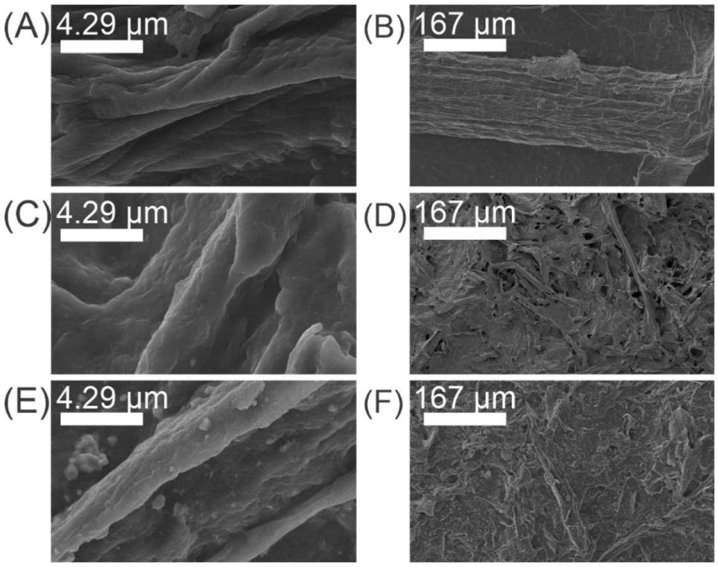

Figure 6. The high-resolution FE-SEM images show the cellulose fibrils in the left column and sample morphology on the right for the cut stem control (A and B), stems after being milled for 2 minutes (C and D), and 15 minutes (E and F).

Very different results appear after milling cellulose fibrils for 15 minutes at 30 Hz in this study with previous work on milled cotton.[5] Here for sorghum, more intact fibril morphology is maintained when milling the cellulose fibrils within a second plant cell wall (Figure 6E, Ling et al. 2019). In the Ling et al. 2019 study, cotton cellulose was fractured to the point microfibril structures were obscured and fibril chunks remained. There was qualitatively less severe cracking on the surface of fibrils in Figure 6E in the plant cell wall sorghum sample in this study and general fibril shapes are still apparent.

In this current study, initial morphology of the intact cellulose fibrils in the plant cell wall was approached with FE-SEM and other techniques which may be considered for future evaluation of cellulose fibril structure within the heterogeneous plant cell wall during deconstruction for sorghum stems. Other techniques may yield further information related to recalcitrance due to lowered accessible cellulose fibril surfaces available for digestion.

In the future, one class of attractive microscopies is vibrational microscopy (using Raman or IR) for verifying cellulose including crystalline and amorphous cellulose[5,40]. However, implementing these techniques suffer from the complexity of an intact plant cell wall and cellulose fluorescence.[40,40,106] The

benefit of microscopy over spectroscopy for assessing cellulose in the plant cell wall is the arrangement of the polymer in cellulose fibrils which vary in orientation and direction so techniques which can focus on one cellulose fibril at a time are favorable. Techniques such as Confocal Raman Spectroscopy with a 785 nm or 1064 nm lasing source or AFM-IR would both require optical arrangements suitable for detection of cellulose signals between 3000-400 cm^{-1} for informing on the cellulose fibril structure and on lignin or hemicellulose on cellulose fibril surfaces relevant for recalcitrance.[40,107,108] Vibrational microscopy would also have the advantage of confirming cellulose as the cellulose fibril structure is obscured in deconstruction. However for the scope of this current study includes FE-SEM structures were confirmed using literature[98] and the assertion of cellulose predominance in the plant cell wall.[1,24]

Atomic Changes in Cellulose Fibril Structure

For sorghum secondary plant cell walls subjected to vibratory milling, recalcitrance would be supported by the correlated decrease of crystalline cellulose and an increase in rigid amorphous cellulose. Such details can be extracted experimentally on the cellulose fibril structure using 2D solid-state NMR (Figure 7 and Figure 8). Molecular insights specific to the constitution and state of the cellulose fibrils was assessed with CP-PDSD experiments with a 1500 ms and 30 ms mixing times to assess crystallinity.[24,68] Peaks in the CP-PDSD were assigned using previously characterized peaks for polymers in the sorghum secondary plant cell wall *Gao et al. 2020* (see Table S1) and signals consistent with the CP-rINADEQUATE experiment for each dimension (Figures 7A, 8A and 9C). Cross peaks in the CP-PDSD experiment represent rigid dipolar (through space coupling) (Figures 7A and 8A).

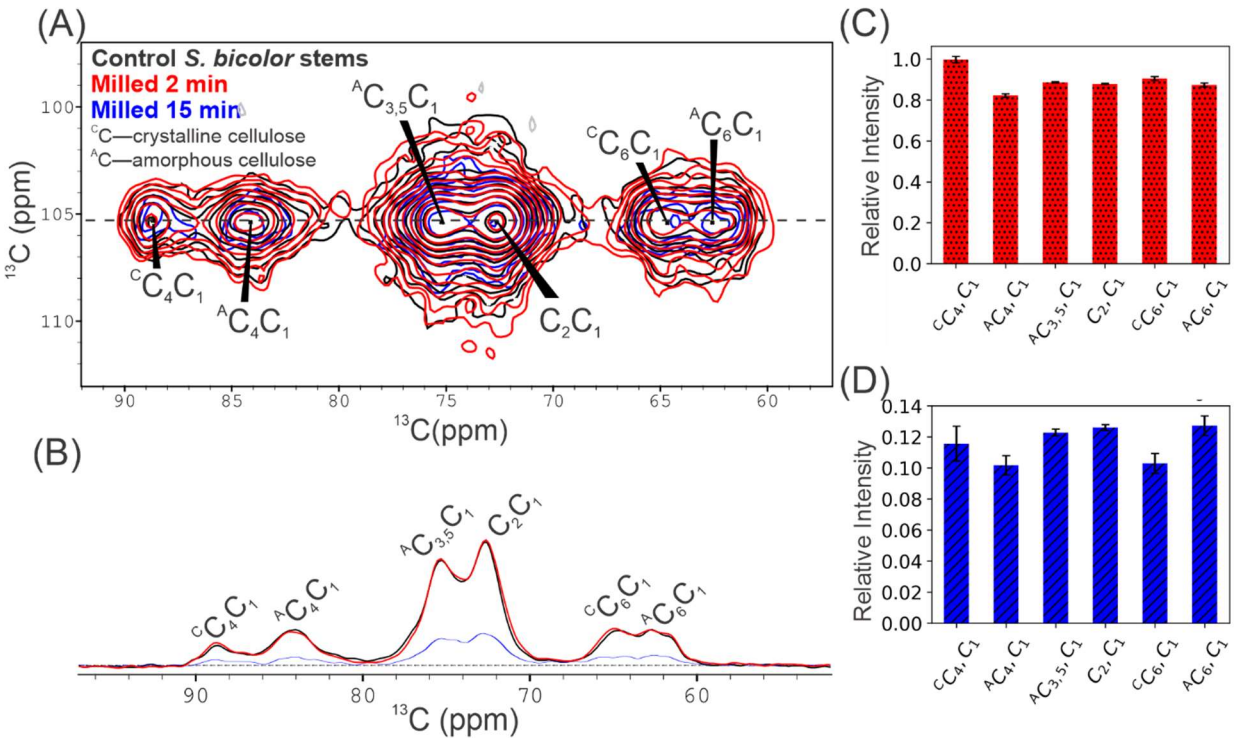

Figure 7. The cut stem control is presented in black, stems milled for 2 minutes in red, and 15 minutes in blue. The carbon 1 region of the 1500 ms 2D CP-PDSD highlights magnetization transfers between carbons 1 through 6 of each D-glucose monomer between all polymers of the cellulose fibrils in the sample (A). A 1D slice from the 1500 ms 2D CP-PDSD at 105.2 ppm in the indirect dimension is taken to demonstrate overall signal intensity change for the magnetization transfers of carbon 1 to the carbons 1 through 6 of the D-glucose monomer (B). The integrated intensity changes in the 1500 ms 2D CP-PDSD relative to the control in panels C and D have a standard deviation estimated with the noise and scaling based on the total ^{13}C content from the 30 s 1D-DP. The carbon 1-6 transfers are represented for stems milled for 2 minutes (C) and the stems milled for 15 minutes (D).

The CP based experiments filter for more rigid components of the secondary plant cell wall because the ^{1}H-^{13}C magnetization transfers are more efficient for rigid spins.[32] The mixing times of the CP-PDSD has a proportional timescale to the distance of the spins between ^{13}C-^{13}C through space.[32] The downside of the experiment is the broader line shapes due to heterogeneous line broadening from spins in multiple orientations coupling at similar frequencies, but crucial information about the cellulose fibril morphologies can still be obtained. The 1500 ms mixing period for the 1500 ms 2D CP-PDSD experiment reports on the larger cellulose structure along fibrils and between fibrils (Figure 7). The 30 ms CP-PDSD 30 experiment has a mixing time of 30 ms where there is enough time for the magnetization transfers to pass between the carbons within the glucose sugar of the monomer of the cellulose fibrils in Figure 8.[24]

First examination of the cellulose fibril shows magnetization transfers between D-glucose monomers of cellulose polymers in the 1500 ms CP-PDSD experiment (Figure 2, Figure 7). Cellulose carbon 1 to carbon 2 transfers have the same chemical shifts across both amorphous and crystalline cellulose (Figure 7). The reductions in overall signal intensity considering sample load is negligible after 2 minutes of milling and >88% after 15 minutes of milling. This makes sense as cellulose fibrils appear to be broken down into smaller microparticle fragments. According to the FE-SEM images (Figure 6E and Figure 6F) there may be fewer dipolar coupling-based magnetization transfers available along and between cellulose polymers after 15 minutes of milling.

The proportional intensity changes between amorphous and crystalline cellulose signals of carbon 1 to 4 and carbon 1 to 6 magnetization transfers were assessed in the CP-PDSD experiments to identify the conversion of crystalline cellulose to amorphous cellulose (cellulose recalcitrance Figure 5B). The proportion of the crystalline to amorphous cellulose for the glucose carbon 1 to carbon 4 transfer appears to decrease more for the 2-minute milling period, to 99.70 ± 1.59% and 82.17 ± 0.88% respectively of the relative peak intensity before milling (Figure 7C, Table S5). The signal intensity for the crystalline cellulose (11.55 ± 1.12%) and amorphous cellulose (10.16 ± 0.62%, Table S5) appear to be nearly equal for the glucose carbon 1 to carbon 4 after 15 minutes of milling (Figure 7D). The cellulose carbon 4 is of particular relevance as the amorphous cellulose has a chemical shift around 84 ppm and the crystalline cellulose has a chemical shift around 89 ppm.[24,38,53]

The isolation of cellulose carbon 4 in solid-state NMR spectra makes it a more reliable marker for amorphous and crystalline cellulose because they have less overlap than other peaks (Table S1).[24] After 2 minutes of milling the crystalline cellulose content appears higher than the amorphous cellulose content (Figure 7C) and the trend appears to also hold true for the 15 minute period (Figure 7D). The reduction of amorphous cellulose signal may be due to amorphous cellulose becoming more mobile, resulting in less efficient CP transfer necessary for the 1500 ms CP-PDSD experiment. However, Ling et al. 2019 found that

even within the 1D CP experiments a conversion from crystalline to amorphous cellulose was observable as part of their prediction: crystalline cellulose within cellulose fibrils becomes amorphous upon milling. The conversion of crystalline to amorphous cellulose observed after milling was not consistently observed with sorghum. The ratio of crystalline cellulose to amorphous remains the same in 1500 ms CP-PDSD experiments as larger fibril structures are broken down in the milling process (Figures 6C--F and 7C--D). The proportional intensities of crystalline and amorphous cellulose signals for carbon 1 to 4 remained the same after milling consistently for 2 minutes and 15 minutes at 30 Hz (Figure 7C and Figure 7D). The hypothesis of cellulose increasing recalcitrance was not supported as demonstrated in unambiguous carbon 1 to 4 of cellulose peaks for crystalline and amorphous cellulose.

The 1500 ms CP-PDSD carbon 1 to carbon 6 transfers provide similar insight. The proportion of the crystalline to amorphous cellulose for the glucose carbon 1 to carbon 6 transfer appears to decrease more for the 2-minute milling period, to 90.47 ± 0.90% and 87.38 ± 0.88% respectively (Figure 7C, Table S5). The signal intensity for the crystalline cellulose (10.28 ± 0.64%) and amorphous cellulose (12.71 ± 0.62%) appear to be nearly equal for the glucose carbon 1 to carbon 6 after 15 minutes of milling (Figure 7D, Table S5). Both the carbon 4 and carbon 6 regions highlighted in Figure 7A--B appear to be low in signal intensity and it is worth noting the superposition of the noise over weak, broad peaks could distort the integrations so careful interpretation is necessary (Figure 7).

Although the stems milled for 15 minutes show rigid cellulose within the fibril has greater amorphous cellulose than crystalline cellulose (Figure 7D), the low signal intensity makes this observation somewhat ambiguous. The lower overall signal intensity of the stems milled for 15 minutes means the noise is superimposed over the tops of the peaks, compounding the error in these results (Figure 7B). This factor is particularly relevant for the sample milled for 15 minutes given the signal intensity decreases by at least 80% for all peaks (Figure 7B, Figure 7D, and Table S5). For this purpose, overinterpretation may be a liability when assessing recalcitrance using carbon 6 signals of cellulose in the 2D CP-PDSD experiments

where cellulose carbon 4 chemical shift changes provide more information on recalcitrance due to morphology changes from crystalline to amorphous cellulose.

Where the 1500 ms 2D CP-PDSD can give some insight into the larger cellulose structure, the 30 ms 2D CP-PDSD experiment reports on the D-glucose subunit of the cellulose polymer. Similarly, the 30 ms CP-PDSD experiment showed an overall decrease in cellulose structures was negligible after 2 minutes and >86% after 15 minutes of milling (Table S6). When signal intensity is severely reduced the interpretation of integrations is less reliable due to noise super imposed over the tops of peaks. For this study, the 2D-PDSD experiments, interpretations of carbon 1 to 4 peaks are more reliable than the carbon 1 to 6 signals.

The proportion of the crystalline to amorphous cellulose for the glucose carbon 1 to carbon 4 transfer appears to change more for the 2-minute milling period to 101.53 ± 1.69% and 87.91 ± 1.00%, respectively (Figure 8C, Table S6). The signal intensity for the crystalline cellulose (13.77 ± 1.28%) and amorphous cellulose (11.89 ± 0.76%) appear to be nearly equal for the glucose carbon 1 to carbon 4 after 15 minutes of milling (Figure 8D, Table S6). The proportion of the crystalline to amorphous cellulose for the glucose carbon 1 to carbon 6 transfer appears to decrease more for the 2-minute milling period to 80.28 ± 1.36% and 74.65 ± 1.39%, respectively (Figure 8C, Table S6). The signal intensity for the crystalline cellulose (11.32 ± 1.03%) and amorphous cellulose (11.47 ± 1.06%) appear to be nearly equal for the glucose carbon 1 to carbon 6 after 15 minutes of milling (Figure 8D, Table S6). In the future, dephasing curves could be applied to specifically probe cellulose fiber substructures with the 2D CP-PDSD experiment similar to previous studies on the plant cell walls.[23,24,39] Dephasing curves would give more specific mixing times for the experiment between 30 ms and 1500 ms mixing times of the 2D CP-PDSD experiments. However, for the purpose of exploring the recalcitrant implications of milling where cellulose fibrils are disrupted to accommodate particle sizes smaller than the fibril width 1 µm or length 100 µm, other experiments may be also explored.[18,48,94] Future use of the 30 ms CP-PDSD experiment may be more

suitable for cellulose morphology based on carbon 4 as sizes of cellulose fibrils are reduced and long range CP mixing times becoming more inefficient.

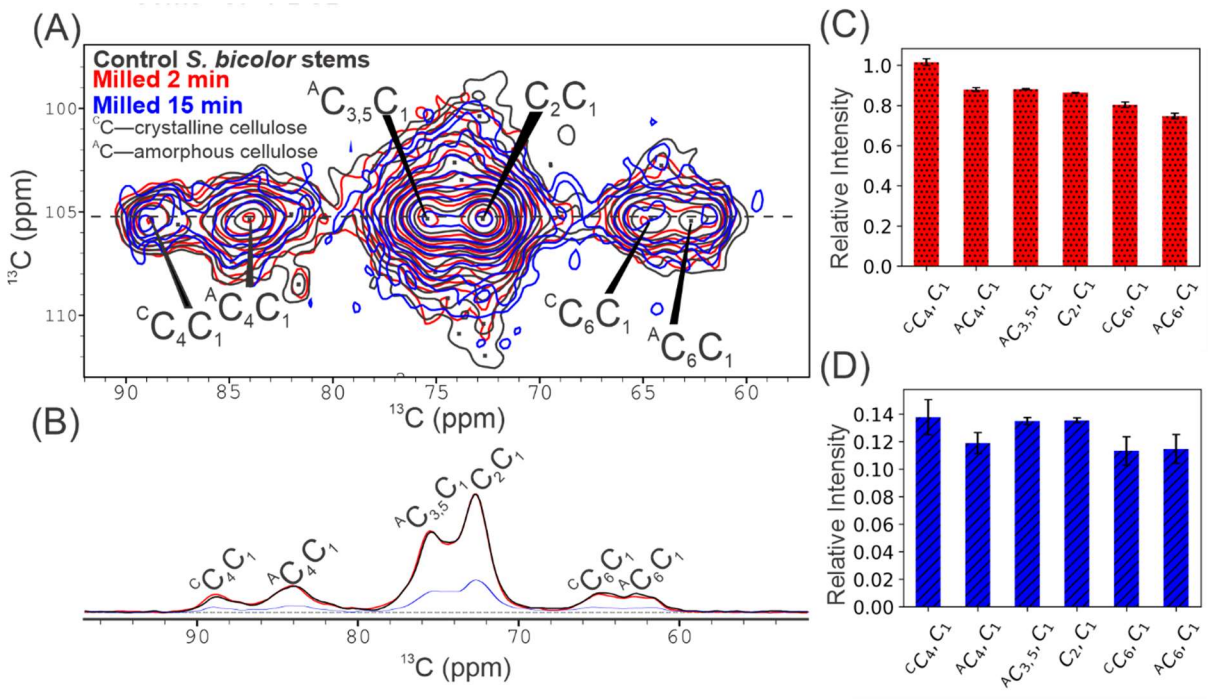

Figure 8. The cut stem control is presented in black, stems milled for 2 minutes in red, and 15 minutes in blue. Cellulose within the cellulose fibrils has a general atomic morphology captured by the 30 ms 2D CP-PDSD, as a more clearly outlined by the carbon 1 region (A). A 1D slice from the 30 ms 2D CP-PDSD at 105.2 ppm in the indirect dimension is taken to demonstrate overall signal intensity change for the magnetization transfers of carbon 1 to the carbons 1 through 6 of the D-glucose monomer (B). The integrated intensity changes of the 30 ms 2D CP-PDSD relative to the control in panels C and D have a standard deviation estimated with the noise and scaling based on the ^{13}C content from the 30 s 1D-DP. The carbon 1-6 transfers in red represent stems milled for 2 minutes (C) and the 15-minute milled stems (D).

After milling, cellulose fibrils are still present in the morphology of the sample (Figure 6) and there is not a reduction in the crystalline cellulose cross-peaks in the 30 ms 2D CP-PDSD (Figure 8). This means that the crystalline morphology of cellulose within the fibril is not directly converted to amorphous cellulose as suggested by analysis milling pure cellulose fibril.[5] The atomic structure of the cellulose fibrils appears to be maintained after milling based on the 30 ms CP-PDSD cellulose one carbon correlations, for example the crystalline cellulose to amorphous cellulose signal intensity ratio was maintained for carbons 4 and 6 (Figure 8C and Figure 8D). Cellulose carbon 4 signals are particularly important because it can offer

insight into the cellulose 1-O-4 polymer backbone of cellulose and chemical shifts which indicate the environment interior through exterior of the cellulose fibril.[1,23,24,29,37,38,58,68,69]

Signals in the 2D CP-rINADEQUATE arise from highly immobilized polymers in the secondary plant cell wall structural hemicellulose and cellulose.[23,24,58] Interpretation of these signals is less straightforward due to resonance overlap for these carbohydrates, but the signals pertaining to the carbon 4 chemical shifts of glucose within cellulose are well resolved (Figure 9, Table S1).[24] The CP-rINADEQUATE shows directly bonded nuclei and is useful for identifying specific subtypes of prominent monomers within the secondary plant cell wall.[23,24,35] The chemical shifts of the bonded nuclei (single quantum coherence) sum to another peak in the indirect dimension shown in the y-axis (the double quantum coherence).[23,24,35] The single quantum (x-axis) chemical shifts were assigned using previously established values of sorghum secondary plant cell wall polymers (Gao et al. 2020) and were verified using crosspeaks (Table S1). Monomers were traced out using crosspeaks because the y-axis double quantum coherence is assigned by a chemical shift from the sum of chemical shifts from two directly bonded ^{13}C spins. Note, the monomers found by the rINADEQUATE are contained within the polymers within the secondary plant cell wall and shifted downfield compared to literature of dry solid monomers and monomers in water.

Many of the unambiguous signals of cellulose all reduced in signal intensity (Figure 9E, Table S1): after 2 minutes of milling the signals reduced by 15% for all unambiguous amorphous cellulose peaks (Figure 9F, Table S7). After 15 minutes of milling the crystalline cellulose signal associated with interior crystalline cellulose within the dehydrated space around 84 ppm of the cellulose fibril decreased nearly to the noise. The signal reduction of the crystalline and amorphous cellulose appeared to be equal suggesting crystalline cellulose did not convert to amorphous cellulose when milled, contrary to pure cellulose as found in Ling *et al.* 2019.[5] However, the remaining crystalline cellulose carbon 4 does not appear to significantly differ in the proportions of decreasing amorphous cellulose 4 for the interior and exterior positions, as noted in Gao et al. 2020. In Figure 9, additional subscripts i to iii refer to the least to the most

dehydrated (interior) cellulose i.e. the interior to exterior polymers in the cellulose fibers based on previous studies.[23,24] Results of the current study show overall signal reduction of the amorphous cellulose after 2 minutes is only around 3% and by 75% after the 15 minutes of milling (Table S7).

Beyond the carbon 4 area of the CP-rINADEQUATE spectrum, cellulose signals often overlap with rigid hemicellulose.[24] The total amount of cellulose estimated by the glucose carbon 1 peak at 105.2 ppm overlaps with many of the hemicellulose carbon 1 peaks including structurally relevant 2-fold xylan (^{2f}Xn) hemicellulose at 105.1 ppm (Table S1). The carbon 1 of cellulose can be less quantitative in the CP-rINADEQUATE compared to the CP-PDSD experiments discussed here. The slice from the carbon 1 region of the CP-rINADEQUATE supports an overall cellulose signal reduction in Figure 9G which is apparent in the overlay of the control, stems milled for 2 minutes, and stems milled for 15 minutes in Figure 9D.

To summarize, there is an overall signal reduction and the proportion of amorphous and crystalline cellulose appear to be maintained after milling in the CP based experiments CP-rINADEQUATE, 30 ms and 1500 ms 2D CP-PDSD experiments. Additional evaluation of the signals using normalized intensities of carbon 1 for the 30 ms CP-PDSD experiment could offer further statistical insight on cellulose within the sample based on changes in monomers, without handling as much signal overlap as the CP-rINADEQUATE. As the cellulose structure is further milled beyond the 1 μm particle size, the amount of information which will be available in the 1500 ms CP-PDSD experiment is expected to decrease and may be removed from the experiment set for more informative experiments. CP becomes less efficient for more liquid like samples and the 1500 ms CP-PDSD has a mixing time suited for distances potentially exceeding cellulose fibril lengths as they are broken down.[32,48] Overall, the argument of increased recalcitrance due to conversion of crystalline to amorphous cellulose using milling is not supported by the CP-PDSD and CP-rINADEQUATE spectra. However, understanding the available digestible cellulose may be more informative especially as hemicellulose and lignin could sit on the surface of cellulose fibrils and reduce available surface area for digestion.[56]

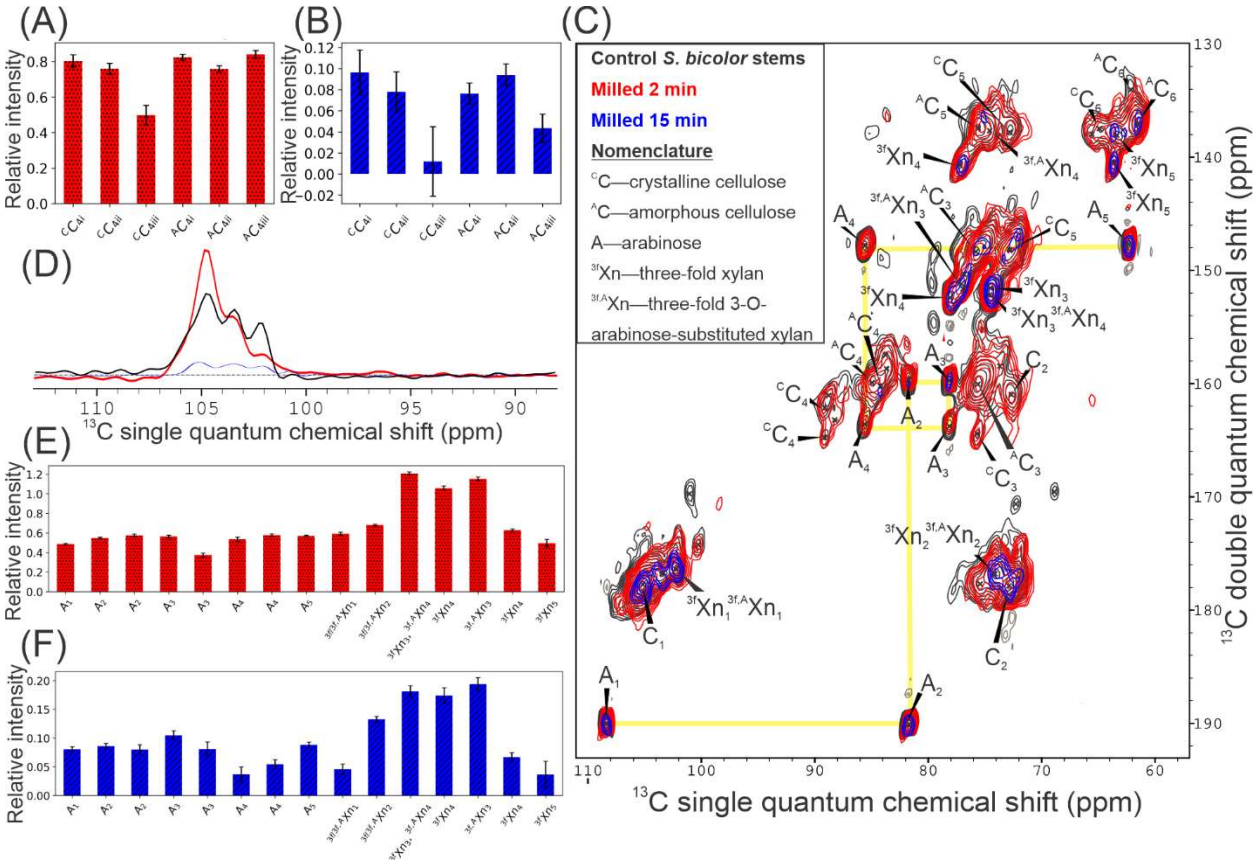

Figure 9. Rigid directly bonded carbons such as those within monomers from polymers including cellulose fibrils and hemicellulose xylan substituted with arabinose and xylan are traceable carbon-carbon bonds in the 2D CP-rINADEQUATE spectrum. Integrated differences of unambiguous peaks for the cellulose carbon 4 peaks for the stems milled for 2 minutes (A) and stems milled for 15 minutes in blue (B). Subscripts i to iii are designated from most hydrated to least hydrated cellulose. In panel C the arabinose carbons 1--5 show how single quantum chemical shits on the x-axis of directly bonded atoms sum to the sample double quantum shift in the y axis, thus enabling full monomer unit to become traceable with arabinose highlighted as an example. The cellulose signal reduction apparent in the overlay control in black, stems milled for 2 minutes in red, and stems milled for 15 minutes in blue (C). Slices from the carbon 1 region of the CP-rINADEQUATE with 1D slices overlayed from the cellulose 1-2 chemical shifts has the control (black) overlayed with the stems milled for 2 minutes (red) and 15 minutes (blue)(D). Changes in structural hemicellulose peak intensities are outlined for the stem milled for 2 minutes in red (E) and 15 minutes in blue(F), both are presented relative to the control.

Hemicellulose Changes After Milling

Structural Hemicellulose Changes After Milling

Signal intensities from arabinose all significantly decrease by at least 30% after ball-milling while 3-fold xylan (^{3f}Xn) carbon 4 and carbon 5 signal intensities increase after 2 minutes (Figure 9H). For the stems milled for 15 minutes, the arabinose intensities decrease by >87%, but are still more prominent than cellulose (Figure 9I, Table S8). After 15 minutes of milling, xylan peaks remained consistently 10% above

the relative intensity of other peaks in the CP-rINADEQUATE (Figure 9I), while cellulose signals frequently dropped below 10% of the relative signal intensity compared to the control (Figure 9I, Table S8). Arabinose serves as a common substitution and a defining feature dictating some xylan interactions with cellulose[24] and is known for facilitating crosslinking between hemicellulose and lignin.[10,60]

The hemicellulose signals appear to remain intact in the 2D CP-rINADEQUATE, although reduce in signal intensity after 15 minutes of ball-milling, meaning that polymers maintain their rigid conformations while the cellulose signals area reduced in the spectra (Figure 9). Hemicellulose signals appear to be more preserved when contrasting overall spectra of the control to the stems milled for 15 minutes (Figure 9D), supporting the structural importance of hemicellulose.[1,10,24] As highlighted in Figure 9C, the arabinose substitutions on rigid hemicellulose signals persist with decreasing intensity in the spectra as presented in the 2D CP-rINADEQUATE overlay.

Observation of xylan hemicellulose in the CP-rINADEQUATE has the same issue of signal overlap as cellulose and only a select number of unambiguous chemical shifts (Table S1), but tracing the full monomers within the spectra helps with some deconvolution. Another note is the predominant xylan-cellulose interaction between the 3-fold xylan and the amorphous cellulose surfaces in sorghum: it is not necessarily expected to increase as amorphous cellulose did not appear to increase. The ^{2f}Xylan that interacts with crystalline cellulose surfaces exhibits heavy signal overlap and has a lower prominence (lower signal) in sorghum secondary plant cell walls.[24] Findings from this study appear to confirm that the use of filtered DP-rINADEQUATE could assist in detecting semirigid hemicellulose structures relative to cellulose.[30,33,39] It is inconclusive whether hemicellulose is creating recalcitrant interactions in the current 2D CP-rINADEQUATE, however remaining structural hemicellulose is more rigid than cellulose in the secondary plant cell wall.

Dynamic Hemicellulose Changes During Milling

The line shapes are generally narrower for the dynamic polymers captured in the ^{1}H-^{13}C 2D rINEPT experiment. To better understand how this is possible, note that spins have an equilibrium aligning their precession along the applied magnetic field (i.e. 500 MHz ^{1}H / 125 MHz ^{13}C) and realign their precessions through longitudinal (T_1) and transverse (T_2) relaxation to the applied magnetic field after RF pulses.[32] In solid-state NMR this relaxation of spins back to equilibrium is typically limited by T_2 relaxation.[33] In the experiment dynamic peaks have a greater signal intensity thanks to the long periods between pulses which captures the long relaxation (of T_1 and T_2) dynamic spins in liquid-like samples and the signals arising from short T_2 relaxations predominating rigid spins are not captured.[33] So, some heterogeneous line broadening from rigid signals and dynamic signals overlap at similar chemical shifts in the rINEPT. And as the more dynamic signals are captured, narrower lines are also observed because the random motion of the spins allows some proton chemical shifts to be canceled out (reduced homogeneous line broadening). Directly bonded ^{13}C and ^{1}H are probed through J-coupling delays between pulse excitations for each nucleus (further detail of the pulse sequence and the dynamics can be found in Spiess (2007) and Matlahov and van der Wel (2018)).

The assignment of the ^{1}H-^{13}C 2D rINEPT was possible given the chemical shifts of polymers identified in the sorghum plant cell wall by *Gao et al. 2020* (Table S1) and previous work examining pectic hemicelluloses in Wang *et al.* 2014(Table REFS, Figure 9). It is worth noting that in this work, the arabinose at 108 ppm was confirmed using the control DP-rINADEQUATE experiment (Figure S3B and S3E). Historically, the monomer chemical shifts are up field of the polymer chemical shifts, computational modeling in silico was used to confirm chemical shifts of xylan and its symmetry, and polymer chemical shifts tend to remain consistent between solid state NMR experiments even if line broadening needs to be considered.[23,29] Some challenges are associated with identifying hemicellulose in the carbon 1 region of the 2D rINEPT as the peaks aside from Arabinose coincide with chemical shifts assigned for pectin and

hemicellulose found in the primary plant cell wall, which is disputed in the secondary plant cell wall and it is challenging to distinctly separate polymers thus far between regions of the primary and secondary plant cell wall. For these reasons, full interpretation of the 2D-rINEPT beyond a fingerprint requires further research.

Using general chemistry knowledge of ^{1}H chemical shifts information the carbon 1 region was supported by the ether chemical shifts typical around 5 ppm consistent with sugar backbones (1-O-4 hemicellulose linkages). The proton chemical shifts inform the assignments of protons within lignin networks. As seen in Figure S3 for the freeze-thaw experiment, the protons of the secondary plant cell wall range from aliphatic shifts to protons in conjugated aromatic systems in the ^{1}H range of 3 ppm to 10 ppm for the plant cell wall polymer ^{13}C chemical shift range of 170 to 60 ppm. Perhaps future work with ^{13}C-^{13}C rINADEQUATE or more dynamic J-coupled experiments could extract information on the number of sub environments monomers, polymers, and substitutions of hemicellulose. This information would be particularly useful in deconstruction to assess the changes in ^{1}H chemical shifts after preprocessing methods such as oxidation and acid treatment used in plant cell wall samples to solubilize cellulose. [22,84,86,109,110] Crosspeaks are not assigned in the 2D rINEPT for ^{1}H because they are continuing to be assigned for the plant cell wall and the correlation of ^{1}H to ^{13}C peaks only accounts for directly bonded nuclei, not double quantum coherences as seen in the CP-rINADEQUATE Figure 9C.

The ^{1}H-^{13}C 2D rINEPT fingerprint (Figure 10A) of highly dynamic hemicellulose generally changes over the milling period. Carbon 1 of arabinose hemicellulose substitutions demonstrate a change in the number of proton environments over the milling process and a reduction in signal intensity (Figure 10A and Figure 10B). The carbon 1 of arabinose substitutions of hemicellulose decreases to 39.35 ± 3.92% and pectic hemicellulose to 29.62 ± 1.62% after 2 minutes of milling. Arabinose carbon 1 of arabinose substitutions on structural hemicellulose 14.81 ± 2.23% and pectic hemicellulose 5.69 ± 0.92% after 15

minutes of milling (Table S9). This interpretation of lost signals in Figure 10 suggests that some highly dynamic lignin and hemicellulose (i.e. arabinose) could become less dynamic.

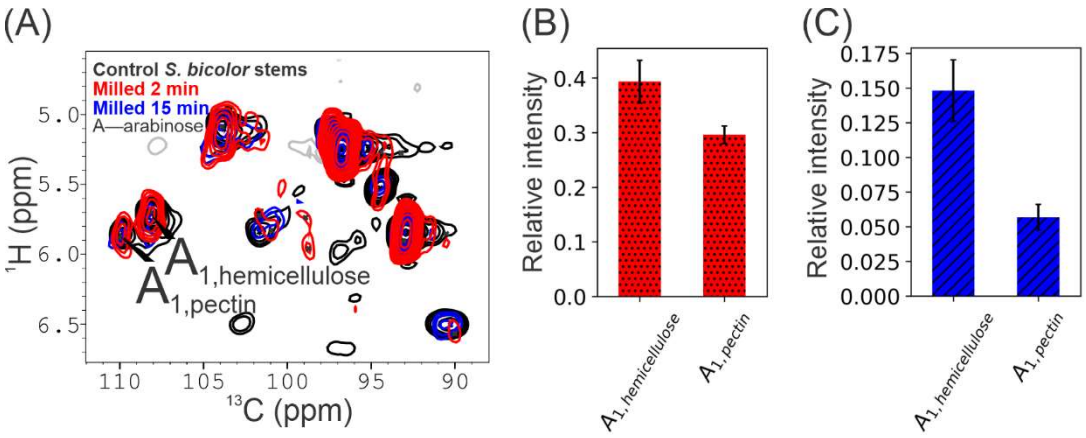

Figure 10. Dynamic hemicellulose signals for the pectic and hemicellulose arabinose are assigned in the ^{1}H-^{13}C 2D rINEPT spectra with the carbon chemical shift on the x axis and the proton chemical shift on the y axis, with the control in black, stems milled for 2 minutes in red and stems milled for 15 minutes in blue (A). The relative signal intensity changes in the stems milled for 2 minutes in (B) and stems milled for 15 minutes in (C).

Further, the reduction of arabinose hemicellulose substitution signals in the CP-rINADEQUATE and in the rINEPT of polymers together suggest that arabinose, and arabinose substituted hemicellulose (^{3f,A}Xylan) takes on a more intermediate dynamic in the plant cell wall. Tracking arabinose substitutions may show a potential marker for rigid and dynamic hemicellulose changes related to recalcitrance. Additionally, the recalcitrance hypothesis based on structural hemicellulose maintaining their rigidity is supported as signals are stronger for arabinose and ^{3f,A}Xylan remain in the CP-rINADEQUATE experiment (Figures 9C and 9E--F).

Lignin Changes in the Plant Cell Wall Matrix During Milling

Reduction in lignin signals would indicate a loss of mobility associated with lignin condensation and emerging lignin cross-linkages are noted in the rINEPT experiment.[111] Interpretation of ^{13}C rINEPT signals was possible after utilization of the DP-rINADEQUATE for the initial assignment of dynamic directly bonded carbons. Examination of the lignin fingerprint of the rINEPT (Figure 11A) reveals one predominant change standing out in the upper portion of the Figure 11A. A dominant lignin ether linkage is present in

the control, reduced in intensity for the 2-minute ball-milling timepoint, and then lost after 15 minutes of ball-milling (Figure 11B and Figure 11C).

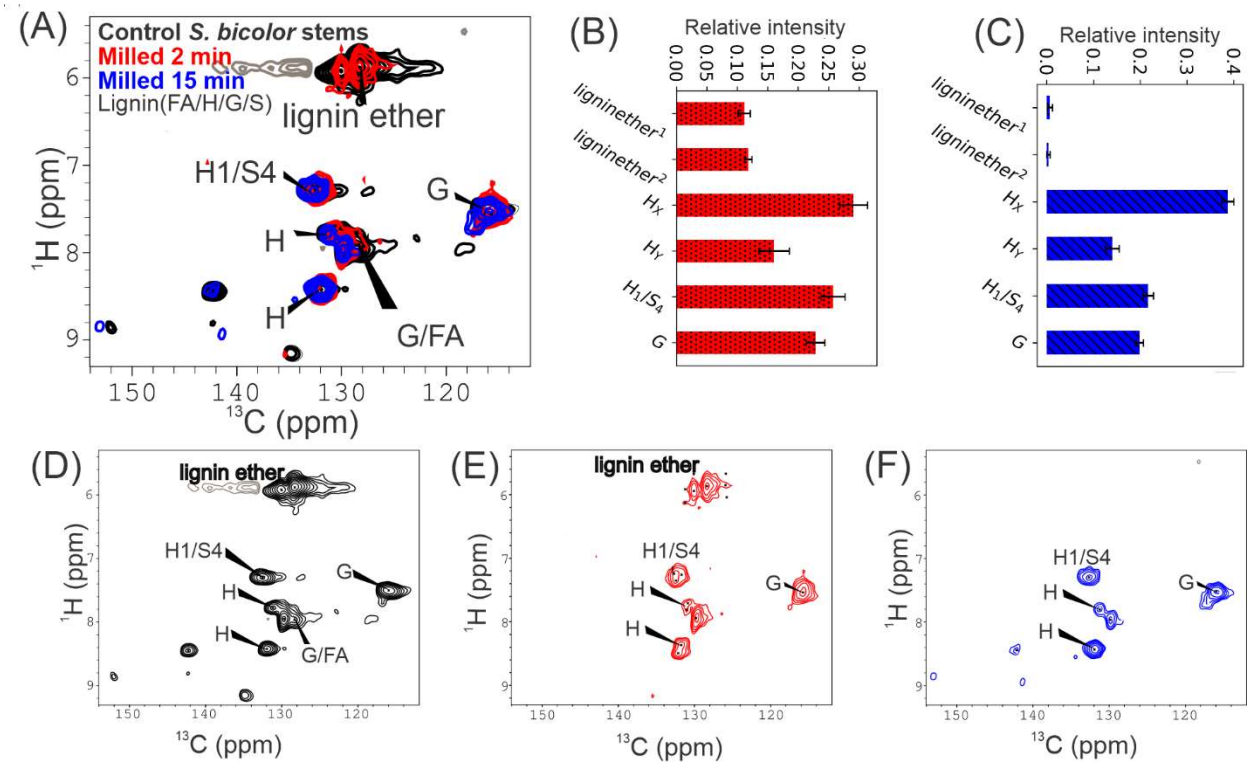

Figure 11. Dynamic lignin signals in the 2D rINEPT signals are outlined including lignin ether signal (A). The control is in black, stems milled for 2 minutes in red and 15 minutes in blue for the overlay (A). The initial assignment of peaks is only displayed in (A) with unambiguous signal intensities highlighted for the stems milled for 2 minutes in red (B) and stems milled for 15 minutes in blue (C). The 2D rINEPT spectra are separated in panels D--F for the control, stems milled for 2 minutes and 15 minutes, respectively.

Upon integration, the ether linkage signal intensity decreases by more than 85% after 2 minutes of milling and by more than 98% after 15 minutes of milling, approaching the noise level of the spectra (Figure 11B, Figure 11C, and Table S9). The reduction in the lignin signals and the loss of the ether peak in the rINEPT spectra are interpreted as lignin becoming less mobile. The H lignin signal only decreases by around 60% for both the milled samples, whereas the other dynamic lignin signals decrease by more than 70% after 2 minutes of milling and by more than 85% after 15 minutes of milling (Figure 11B, Figure 11C, and Table S9). In the future, highly dynamic carbon-carbon correlated rINEPT or other experiments would be more informative for both assignments and signal changes given lignin's irregularities as a

heteropolymer and to assess the ether linkage changing due to lignin-lignin ether linkages such as the prominent β-O-4 linkage (Figure 4B) or the cross-linkages reported for arabinose and lignin (Figure 3B).[60]

Mechanically Induced Milling Recalcitrance by Vibratory Milling

The 30 ms CP-PDSD and the CP-rINADEQUATE does not show crystalline cellulose becoming more amorphous based on carbon 4 of cellulose (Figure 8C, Figure 8D, Figure 8E, and Figure 8F). The FE-SEM still shows fibril structures (Figure 6), meaning that the cellulose fibrils appear to be breaking down into smaller cellulose fibril particulates with the same atomic structure of cellulose arrangements, as found in the native secondary plant cell wall structure. Mechanically induced recalcitrance from cellulose changing morphology from crystalline to amorphous during milling was not supported. However, the changes detected in the rINEPT and CP MAS-ssNMR experiments gave insight into the of highly dynamic and rigid polymer changes, supporting hemicellulose reorganization of the secondary plant cell wall polymers. Recalcitrant markers of the lignin ether linkage and arabinose polymer mobility reduction appear prevalent in the rINEPT after vibratory ball-milling. Mechanically induced recalcitrance from lignin activation, crosslinking, and condensation of polymers lignin and hemicellulose can be further investigated as markers for recalcitrance using MAS-ssNMR studies tailored for detecting intermediately dynamic polymers in the samples.

Chapter 5: Outlook and Conclusion

Efficient ^{13}C labeling of living plants has increased the understanding of how biopolymer organization within the plant cell wall confers biomass recalcitrance. Since solid-state NMR does not require solubilization of the plant cell wall, access to ^{13}C labeled plant material allows for the native secondary plant cell wall architecture to be tracked during biomass conversion at high resolution. Evaluation of the changes within the 2D spectra need to be carefully considered within the context of the complex matrix and the selected unambiguous peaks (Table S1) and the consistency of changes as they occur upon integration for all the experiments moving forward (Tables S5-13).

Of the hypothesized recalcitrance laid out in Figure 5, the recalcitrance from crystalline cellulose converting to amorphous cellulose was not within rigid structures detected by CP experiments. After 15 minutes of milling the reduction of cellulose signals ranged between 80-85% (Table S7). Furthermore, CP based experiments may suffer from lower signal-to-noise ratio in future experiments for sorghum as cellulose fibrils are reduced to substructures and samples take on a more liquid consistency. Details provided by cellulose carbon 4 served as a marker for polymer morphology changes in the CP experiments (Figures 6--9). However, it is worth noting that the reduction of particle size limits the effectiveness of 2D CP-PDSD experiments with long mixing times and beyond 15 minutes of milling the 1500 ms 2D CP-PDSD could be exchanged for a more informative experiment.

Hemicellulose appeared to maintain more signal intensity than the cellulose structures for structural hemicellulose in the CP-rINADEQUATE (Figure 9). This supports the recalcitrance hypothesis in Figure 5C given particularly high ^{3f}Xylan, and arabinosyl substitutes of hemicellulose remaining. The clearest marker was arabinosyl groups implicated in xylan-lignin crosslinking (Figures 3F, 5C, 9, and 10). A reduction in ^{3f}Xylan and highly dynamic signals in the ^{1}H-^{13}C 2D rINEPT was expected as additional hemicellulose associating with amorphous cellulose would make the polymer more rigid (and higher proton decoupling would be needed to see the signal). More data is needed to deconvolute the rINEPT and assign highly dynamic signals for sorghum. Work here would support the “upper bound” of highly dynamic components of the secondary plant cell wall. However, one cursory marker remains well defined: the arabinosyl hemicellulose substitution which defines the xylan morphology[24,58] has a high prevalence in the sorghum plant cell wall[6,10,24] and is implicated in cross-linkages between hemicellulose and lignin especially xylan[10,60].

In the ^{1}H-^{13}C 2D rINEPT, the carbon 1 arabinosyl maintains good separation between hemicellulose (~108 ppm) and pectic (~110 ppm) decorations (Table S2, Figure 10A). The reduction of arabinosyl substitutions for dynamic hemicellulose suggests some rigidification for hemicellulose substitutions with

arabinosyl subunits. Further J-coupling based 2D experiments to assign directly bonded carbon may support hemicellulose changes and perhaps how lignin condensation could influence structural xylan crosslinked to lignin through xylan-arabinose-lignin linkages and other linkages.

The overall reduction in lignin signals from the highly dynamic ^{1}H-^{13}C 2D rINEPT after milling supports lignin condensation, considering a reduction in dynamics could result in signal loss. The loss of the ether signal in the rINEPT supports this and incentivizes its characterization as a recalcitrance marker due to both the hemicellulose crosslinkages (Figures 3F, 5C) and the lignin β-O-4 linkage (Figure 4E) targeted in deconstruction techniques. [3,7,86] Expanding on the lignin characterization in (Table S3--4, Figure S4) would be one method of locating other lignin linkages and crosslinkages with DP experiments and the rINEPT. Unsurprisingly, recalcitrance due to lignin condensation is supported from Figure 5D.

Chemical shift changes after milling can be further evaluated for the solid-state NMR data collected in this work. The 2D integrations (Tables S10-13) and future analysis in NMRpipe are possible because NMR data was collected using consistent parameters, allowing data to be plotted on the same spectral grid. After the integration, some markers for recalcitrance (Figure 5) are highlighted and more detailed chemical shift changes can be evaluated. for cellulose carbon 4, arabinose as well as the xylan signals in the CP-rINADEQUATE, and lignin rINEPT signals. Future analysis utilizing spectral subtraction in NMRpipe[100] could more distinctly confirm peak shifts and changes in light of the heterogeneous line broadening in the spectra.

Further research is needed to explore the mechanical preprocessing step of the deconstruction pathway as a source of mechanically induced recalcitrance, and methods to overcome recalcitrance require additional experiments. Sorghum wild-type leaves and roots can provide references for mechanical induced recalcitrance as the secondary plant cell wall content varies through the stems, leaves, and roots. Contrasts between tissue types containing more and less secondary plant cell wall (e.g. comparing stem

and leaf tissue) will also aid in assessing lignin associated recalcitrance. Genetic engineering efforts based on a molecular understanding of recalcitrance could also prove invaluable.[86,112,113] Capacities to overcome mechanical induced recalcitrance in deconstruction pathways through low lignin mutations in sorghum and by performing whole plant digestion such as in ionic liquid deconstruction pathways[89] can be explored with MAS-ssNMR and FE-SEM. Future use of vibrational microscopy such as confocal Raman or AFM-IR may help assess recalcitrance caused by loss of digestible cellulose fibril surfaces.[40,48,56,106]

Future MAS-ssNMR experiments to probe recalcitrance molecular markers in DP experiments (which excite all ^{13}C nuclei in the sample) can be adjusted so that rigid polymer signals are filtered[33]. Increased recycle delays (time between scans), selective excitation, and lowered proton decoupling powers may allow the selection of polymers with intermediate mobility. The filtered-DP-rINADEQUATE could more accurately assess changes in dynamic polymers which might then improve the rINEPT assignments. Filtered DP-PDSD experiments could improve assessment of intramolecular and intermolecular interactions assessment of hemicellulose and lignin interactions. There is potential for adapting filtered DP-PDSD experiments with dephasing curves to extract changes in physical distances between polymers.[80] Although more sophisticated analyses and a wider variety of NMR experiments are possible, the current example highlights the power of solid-state NMR to detect structural changes during lignocellulosic biomass conversion.

Bibliography

(1) Marriott, P. E.; Gómez, L. D.; McQueen-Mason, S. J. Unlocking the Potential of Lignocellulosic Biomass through Plant Science. *New Phytol.* **2016**, *209* (4), 1366–1381. https://doi.org/10.1111/nph.13684.

(2) Langholtz, M. H.; Stokes, B. J.; Eaton, L. M. 2016 Billion-Ton Report: Advancing Domestic Resources for a Thriving Bioeconomy, Volume 1: Economic Availability of Feedstock. *OAK RIDGE Natl. Lab. Oak RidgeTennessee Manag. UT-Battelle LLC US Dep. ENERGY* **2016**, *2016* (Vol. 1), 1–411.

(3) Li, T.; Takkellapati, S. The Current and Emerging Sources of Technical Lignins and Their Applications. *Biofuels Bioprod. Biorefining* **2018**, *12* (5), 756–787. https://doi.org/10.1002/bbb.1913.

(4) Westerhof, R. J. M.; Oudenhoven, S. R. G.; Hu, X.; Heeres, H. J.; Li, C.-Z.; Garcia-Perez, M.; Kersten, S. R. A. Biofuel and Methyl Levulinate from Biomass-Derived Fractional Condensed Pyrolysis Oil and Alcohol. *Energy Technol.* **2017**, *5* (1), 205–215. https://doi.org/10.1002/ente.201600389.

(5) Ling, Z.; Wang, T.; Makarem, M.; Santiago Cintrón, M.; Cheng, H. N.; Kang, X.; Bacher, M.; Potthast, A.; Rosenau, T.; King, H.; Delhom, C. D.; Nam, S.; Vincent Edwards, J.; Kim, S. H.; Xu, F.; French, A. D. Effects of Ball Milling on the Structure of Cotton Cellulose. *Cellulose* **2019**, *26* (1), 305–328. https://doi.org/10.1007/s10570-018-02230-x.

(6) Stoklosa, R. J. Deriving Biofuels and Value-Added Co-Products from Sorghum Bicolor: Prospects in Biorefinery Applications and Product Development. In *Innovative Uses of Agricultural Products and Byproducts*; ACS Symposium Series; American Chemical Society, 2020; Vol. 1347, pp 43–62. https://doi.org/10.1021/bk-2020-1347.ch003.

(7) Sun, S.-L.; Wen, J.-L.; Ma, M.-G.; Sun, R.-C. Structural Elucidation of Sorghum Lignins from an Integrated Biorefinery Process Based on Hydrothermal and Alkaline Treatments. *J. Agric. Food Chem.* **2014**, *62* (32), 8120–8128. https://doi.org/10.1021/jf501669r.

(8) Cosgrove, D. J. Growth of the Plant Cell Wall. *Nat. Rev. Mol. Cell Biol.* **2005**, *6* (11), 850–861. https://doi.org/10.1038/nrm1746.

(9) White, P. B.; Wang, T.; Park, Y. B.; Cosgrove, D. J.; Hong, M. *Water–Polysaccharide Interactions in the Primary Cell Wall of Arabidopsis thaliana from Polarization Transfer Solid-State NMR*. ACS Publications. https://pubs.acs.org/doi/pdf/10.1021/ja504108h (accessed 2021-08-01). https://doi.org/10.1021/ja504108h.

(10) Scheller, H. V.; Ulvskov, P. Hemicelluloses. *Annu. Rev. Plant Biol.* **2010**, *61* (1), 263–289. https://doi.org/10.1146/annurev-arplant-042809-112315.

(11) Burgert, I.; Fratzl, P. Plants Control the Properties and Actuation of Their Organs through the Orientation of Cellulose Fibrils in Their Cell Walls. *Integr. Comp. Biol.* **2009**, *49* (1), 69–79. https://doi.org/10.1093/icb/icp026.

(12) Zhang, B.; Gao, Y.; Zhang, L.; Zhou, Y. The Plant Cell Wall: Biosynthesis, Construction, and Functions. *J. Integr. Plant Biol.* **2021**, *63* (1), 251–272. https://doi.org/10.1111/jipb.13055.

(13) van Putten, R.-J.; van der Waal, J. C.; de Jong, E.; Rasrendra, C. B.; Heeres, H. J.; de Vries, J. G. Hydroxymethylfurfural, A Versatile Platform Chemical Made from Renewable Resources. *Chem. Rev.* **2013**, *113* (3), 1499–1597. https://doi.org/10.1021/cr300182k.

(14) Baral, N. R.; Sundstrom, E. R.; Das, L.; Gladden, J.; Eudes, A.; Mortimer, J. C.; Singer, S. W.; Mukhopadhyay, A.; Scown, C. D. Approaches for More Efficient Biological Conversion of Lignocellulosic Feedstocks to Biofuels and Bioproducts. *ACS Sustain. Chem. Eng.* **2019**, *7* (10), 9062–9079. https://doi.org/10.1021/acssuschemeng.9b01229.

(15) Genuino, H. C.; Muizebelt, I.; Heeres, A.; Schenk, N. J.; Winkelman, J. G. M.; Heeres, H. J. An Improved Catalytic Pyrolysis Concept for Renewable Aromatics from Biomass Involving a Recycling Strategy for Co-Produced Polycyclic Aromatic Hydrocarbons. *Green Chem.* **2019**, *21* (14), 3802–3806. https://doi.org/10.1039/C9GC01485C.

(16) Priharto, N.; Ronsse, F.; Yildiz, G.; Heeres, H. J.; Deuss, P. J.; Prins, W. Fast Pyrolysis with Fractional Condensation of Lignin-Rich Digested Stillage from Second-Generation Bioethanol Production. *J. Anal. Appl. Pyrolysis* **2020**, *145*, 104756. https://doi.org/10.1016/j.jaap.2019.104756.

(17) Talmadge, K. W.; Keegstra, K.; Bauer, W. D.; Albersheim, P. The Structure of Plant Cell Walls: I. The Macromolecular Components of the Walls of Suspension-Cultured Sycamore Cells with a Detailed Analysis of the Pectic Polysaccharides. *Plant Physiol.* **1973**, *51* (1), 158–173. https://doi.org/10.1104/pp.51.1.158.

(18) Kim, H.; Ralph, J. Solution-State 2D NMR of Ball-Milled Plant Cell Wall Gels in DMSO-D6/Pyridine-D5. *Org. Biomol. Chem.* **2010**, *8* (3), 576–591. https://doi.org/10.1039/B916070A.

(19) Zhang, R.; Qi, Y.; Ma, C.; Ge, J.; Hu, Q.; Yue, F.-J.; Li, S.-L.; Volmer, D. A. Characterization of Lignin Compounds at the Molecular Level: Mass Spectrometry Analysis and Raw Data Processing. *Mol. Basel Switz.* **2021**, *26* (1), E178. https://doi.org/10.3390/molecules26010178.

(20) Nishiyama, Y.; Langan, P.; Chanzy, H. Crystal Structure and Hydrogen-Bonding System in Cellulose Iβ from Synchrotron X-Ray and Neutron Fiber Diffraction. *J. Am. Chem. Soc.* **2002**, *124* (31), 9074–9082. https://doi.org/10.1021/ja0257319.

(21) Li, M.; Pu, Y.; Ragauskas, A. J. Current Understanding of the Correlation of Lignin Structure with Biomass Recalcitrance. *Front. Chem.* **2016**, *4*, 45. https://doi.org/10.3389/fchem.2016.00045.

(22) Gilna, P.; Lynd, L. R.; Mohnen, D.; Davis, M. F.; Davison, B. H. Progress in Understanding and Overcoming Biomass Recalcitrance: A BioEnergy Science Center (BESC) Perspective. *Biotechnol. Biofuels* **2017**, *10* (1), 285. https://doi.org/10.1186/s13068-017-0971-1.

(23) Simmons, T. J.; Mortimer, J. C.; Bernardinelli, O. D.; Pöppler, A.-C.; Brown, S. P.; deAzevedo, E. R.; Dupree, R.; Dupree, P. Folding of Xylan onto Cellulose Fibrils in Plant Cell Walls Revealed by Solid-State NMR. *Nat. Commun.* **2016**, *7* (1), 13902. https://doi.org/10.1038/ncomms13902.

(24) Gao, Y.; Lipton, A. S.; Wittmer, Y.; Murray, D. T.; Mortimer, J. C. A Grass-Specific Cellulose–Xylan Interaction Dominates in Sorghum Secondary Cell Walls. *Nat. Commun.* **2020**, *11* (1), 6081. https://doi.org/10.1038/s41467-020-19837-z.

(25) Munson, C. R.; Gao, Y.; Mortimer, J. C.; Murray, D. T. Solid-State Nuclear Magnetic Resonance as a Tool to Probe the Impact of Mechanical Preprocessing on the Structure and Arrangement of Plant Cell Wall Polymers. *Front. Plant Sci.* **2022**, *12*.

(26) Gao, Y.; Mortimer, J. C. Chapter 7 - Unlocking the Architecture of Native Plant Cell Walls via Solid-State Nuclear Magnetic Resonance. In *Methods in Cell Biology*; Anderson, C. T., Haswell, E. S., Dixit, R., Eds.; Plant Cell Biology; Academic Press, 2020; Vol. 160, pp 121–143. https://doi.org/10.1016/bs.mcb.2020.05.001.

(27) Chen, W.-P.; Yang, X.-Y.; Harms, G. L.; Gray, W. M.; Hegeman, A. D.; Cohen, J. D. An Automated Growth Enclosure for Metabolic Labeling of Arabidopsis Thaliana with 13C-Carbon Dioxide - an in Vivo Labeling System for Proteomics and Metabolomics Research. *Proteome Sci.* **2011**, *9* (1), 9. https://doi.org/10.1186/1477-5956-9-9.

(28) Dick-Pérez, M.; Zhang, Y.; Hayes, J.; Salazar, A.; Zabotina, O. A.; Hong, M. Structure and Interactions of Plant Cell-Wall Polysaccharides by Two- and Three-Dimensional Magic-Angle-Spinning Solid-State NMR. *Biochemistry* **2011**, *50* (6), 989–1000. https://doi.org/10.1021/bi101795q.

(29) Dupree, R.; Simmons, T. J.; Mortimer, J. C.; Patel, D.; Iuga, D.; Brown, S. P.; Dupree, P. Probing the Molecular Architecture of Arabidopsis Thaliana Secondary Cell Walls Using Two- and Three-

Dimensional 13C Solid State Nuclear Magnetic Resonance Spectroscopy. *Biochemistry* **2015**, *54* (14), 2335–2345. https://doi.org/10.1021/bi501552k.

(30) Kang, X.; Kirui, A.; Dickwella Widanage, M. C.; Mentink-Vigier, F.; Cosgrove, D. J.; Wang, T. Lignin-Polysaccharide Interactions in Plant Secondary Cell Walls Revealed by Solid-State NMR. *Nat. Commun.* **2019**, *10* (1), 347. https://doi.org/10.1038/s41467-018-08252-0.

(31) Terrett, O. M.; Lyczakowski, J. J.; Yu, L.; Iuga, D.; Franks, W. T.; Brown, S. P.; Dupree, R.; Dupree, P. Molecular Architecture of Softwood Revealed by Solid-State NMR. *Nat. Commun.* **2019**, *10* (1), 4978. https://doi.org/10.1038/s41467-019-12979-9.

(32) Spiess, H. W. Spiess, Hans Wolfgang: Multidimensional Solid State NMR of Polymers. In *eMagRes*; John Wiley & Sons, Ltd, 2007. https://doi.org/10.1002/9780470034590.emrhp0174.

(33) Matlahov, I.; van der Wel, P. C. A. Hidden Motions and Motion-Induced Invisibility: Dynamics-Based Spectral Editing in Solid-State NMR. *Methods* **2018**, *148*, 123–135. https://doi.org/10.1016/j.ymeth.2018.04.015.

(34) Phyo, P.; Hong, M. Fast MAS 1H–13C Correlation NMR for Structural Investigations of Plant Cell Walls. *J. Biomol. NMR* **2019**, *73* (12), 661–674. https://doi.org/10.1007/s10858-019-00277-x.

(35) Lesage, A.; Auger, C.; Caldarelli, S.; Emsley, L. Determination of Through-Bond Carbon−Carbon Connectivities in Solid-State NMR Using the INADEQUATE Experiment. *J. Am. Chem. Soc.* **1997**, *119* (33), 7867–7868. https://doi.org/10.1021/ja971089k.

(36) Takegoshi, K.; Nakamura, S.; Terao, T. 13C–1H Dipolar-Assisted Rotational Resonance in Magic-Angle Spinning NMR. *Chem. Phys. Lett.* **2001**, *344* (5), 631–637. https://doi.org/10.1016/S0009-2614(01)00791-6.

(37) Kono, H.; Erata, T.; Takai, M. Determination of the Through-Bond Carbon−Carbon and Carbon−Proton Connectivities of the Native Celluloses in the Solid State. *Macromolecules* **2003**, *36* (14), 5131–5138. https://doi.org/10.1021/ma021769u.

(38) VanderHart, D. L.; Atalla, R. H. Studies of Microstructure in Native Celluloses Using Solid-State Carbon-13 NMR. *Macromolecules* **1984**, *17* (8), 1465–1472. https://doi.org/10.1021/ma00138a009.

(39) Wang, T.; Hong, M. Solid-State NMR Investigations of Cellulose Structure and Interactions with Matrix Polysaccharides in Plant Primary Cell Walls. *J. Exp. Bot.* **2016**, *67* (2), 503–514. https://doi.org/10.1093/jxb/erv416.

(40) Agarwal, U. P. Analysis of Cellulose and Lignocellulose Materials by Raman Spectroscopy: A Review of the Current Status. *Molecules* **2019**, *24* (9), 1659. https://doi.org/10.3390/molecules24091659.

(41) Zhao, Y.; Man, Y.; Wen, J.; Guo, Y.; Lin, J. Advances in Imaging Plant Cell Walls. *Trends Plant Sci.* **2019**, *24* (9), 867–878. https://doi.org/10.1016/j.tplants.2019.05.009.

(42) Zhao, W.; Fernando, L. D.; Kirui, A.; Deligey, F.; Wang, T. Solid-State NMR of Plant and Fungal Cell Walls: A Critical Review. *Solid State Nucl. Magn. Reson.* **2020**, *107*, 101660. https://doi.org/10.1016/j.ssnmr.2020.101660.

(43) Hilz, H.; de Jong, L. E.; Kabel, M. A.; Schols, H. A.; Voragen, A. G. J. A Comparison of Liquid Chromatography, Capillary Electrophoresis, and Mass Spectrometry Methods to Determine Xyloglucan Structures in Black Currants. *J. Chromatogr. A* **2006**, *1133* (1), 275–286. https://doi.org/10.1016/j.chroma.2006.08.024.

(44) Foston, M. B.; Samuel, R.; He, J.; Ragauskas, A. J. A Review of Whole Cell Wall NMR by the Direct-Dissolution of Biomass. *Green Chem.* **2016**, *18* (3). https://doi.org/10.1039/C5GC02828K.

(45) Jung, S.; Foston, M.; Kalluri, U. C.; Tuskan, G. A.; Ragauskas, A. J. 3D Chemical Image Using TOF-SIMS Revealing the Biopolymer Component Spatial and Lateral Distributions in Biomass. *Angew. Chem. Int. Ed.* **2012**, *51* (48), 12005–12008. https://doi.org/10.1002/anie.201205243.

(46) Qi, Y.; Volmer, D. A. Chemical Diversity of Lignin Degradation Products Revealed by Matrix-Optimized MALDI Mass Spectrometry. *Anal. Bioanal. Chem.* **2019**, *411* (23), 6031–6037. https://doi.org/10.1007/s00216-019-01984-y.
(47) Ding, J.; Yoo, C. G.; Pu, Y.; Meng, X.; Bhagia, S.; Yu, C.; Ragauskas, A. J. Cellulolytic Enzyme-Aided Extraction of Hemicellulose from Switchgrass and Its Characteristics. *Green Chem.* **2019**, *21* (14), 3902–3910. https://doi.org/10.1039/C9GC00252A.
(48) Song, B.; Zhao, S.; Shen, W.; Collings, C.; Ding, S.-Y. Direct Measurement of Plant Cellulose Microfibril and Bundles in Native Cell Walls. *Front. Plant Sci.* **2020**, *11*, 479. https://doi.org/10.3389/fpls.2020.00479.
(49) Ward, K. Crystallinity of Cellulose and Its Significance for the Fiber Properties. *Text. Res. J.* **1950**, *20* (6), 363–372. https://doi.org/10.1177/004051755002000601.
(50) Gardner, K. H.; Blackwell, J. The Structure of Native Cellulose. *Biopolymers* **1974**, *13* (10), 1975–2001. https://doi.org/10.1002/bip.1974.360131005.
(51) Huang, S.; Makarem, M.; Kiemle, S. N.; Hamedi, H.; Sau, M.; Cosgrove, D. J.; Kim, S. H. Inhomogeneity of Cellulose Microfibril Assembly in Plant Cell Walls Revealed with Sum Frequency Generation Microscopy. *J. Phys. Chem. B* **2018**, *122* (19), 5006–5019. https://doi.org/10.1021/acs.jpcb.8b01537.
(52) Phyo, P.; Wang, T.; Yang, Y.; O'Neill, H.; Hong, M. Direct Determination of Hydroxymethyl Conformations of Plant Cell Wall Cellulose Using 1H Polarization Transfer Solid-State NMR. *Biomacromolecules* **2018**, *19* (5), 1485–1497. https://doi.org/10.1021/acs.biomac.8b00039.
(53) Mori, T.; Chikayama, E.; Tsuboi, Y.; Ishida, N.; Shisa, N.; Noritake, Y.; Moriya, S.; Kikuchi, J. Exploring the Conformational Space of Amorphous Cellulose Using NMR Chemical Shifts. *Carbohydr. Polym.* **2012**, *90* (3), 1197–1203. https://doi.org/10.1016/j.carbpol.2012.06.027.
(54) Park, S.; Baker, J. O.; Himmel, M. E.; Parilla, P. A.; Johnson, D. K. Cellulose Crystallinity Index: Measurement Techniques and Their Impact on Interpreting Cellulase Performance. *Biotechnol. Biofuels* **2010**, *3* (1), 10. https://doi.org/10.1186/1754-6834-3-10.
(55) Sisson, W. A. X-Ray Studies of Crystallite Orientation in Cellulose Fibers Natural Fibers. *Ind. Eng. Chem.* **1935**, *27* (1), 51–56. https://doi.org/10.1021/ie50301a012.
(56) Mudinoor, A. R.; Goodwin, P. M.; Rao, R. U.; Karuna, N.; Hitomi, A.; Nill, J.; Jeoh, T. Interfacial Molecular Interactions of Cellobiohydrolase Cel7A and Its Variants on Cellulose. *Biotechnol. Biofuels* **2020**, *13* (1), 10. https://doi.org/10.1186/s13068-020-1649-7.
(57) Fernandes, A. N.; Thomas, L. H.; Altaner, C. M.; Callow, P.; Forsyth, V. T.; Apperley, D. C.; Kennedy, C. J.; Jarvis, M. C. Nanostructure of Cellulose Microfibrils in Spruce Wood. *Proc. Natl. Acad. Sci.* **2011**, *108* (47), E1195–E1203. https://doi.org/10.1073/pnas.1108942108.
(58) Grantham, N. J.; Wurman-Rodrich, J.; Terrett, O. M.; Lyczakowski, J. J.; Stott, K.; Iuga, D.; Simmons, T. J.; Durand-Tardif, M.; Brown, Steven. P.; Dupree, R.; Busse-Wicher, M.; Dupree, P. An Even Pattern of Xylan Substitution Is Critical for Interaction with Cellulose in Plant Cell Walls. *Nat. Plants* **2017**, *3* (11), 859–865. https://doi.org/10.1038/s41477-017-0030-8.
(59) Zhang, L.; Gao, C.; Mentink-Vigier, F.; Tang, L.; Zhang, D.; Wang, S.; Cao, S.; Xu, Z.; Liu, X.; Wang, T.; Zhou, Y.; Zhang, B. Arabinosyl Deacetylase Modulates the Arabinoxylan Acetylation Profile and Secondary Wall Formation. *Plant Cell* **2019**, *31* (5), 1113–1126. https://doi.org/10.1105/tpc.18.00894.
(60) Terrett, O. M.; Dupree, P. Covalent Interactions between Lignin and Hemicelluloses in Plant Secondary Cell Walls. *Curr. Opin. Biotechnol.* **2019**, *56*, 97–104. https://doi.org/10.1016/j.copbio.2018.10.010.
(61) Foston, M.; Ragauskas, A. J. Biomass Characterization: Recent Progress in Understanding Biomass Recalcitrance. *Ind. Biotechnol.* **2012**, *8* (4), 191–208. https://doi.org/10.1089/ind.2012.0015.

(62) Pu, Y.; Cao, S.; Ragauskas, A. J. Application of Quantitative 31P NMR in Biomass Lignin and Biofuel Precursors Characterization. *Energy Environ. Sci.* **2011**, *4* (9), 3154. https://doi.org/10.1039/c1ee01201k.

(63) Balakshin, M.; Capanema, E. On the Quantification of Lignin Hydroxyl Groups With 31P and 13C NMR Spectroscopy. *J. Wood Chem. Technol.* **2015**.

(64) Bergs, M.; Do, X. T.; Rumpf, J.; Kusch, P.; Monakhova, Y.; Konow, C.; Völkering, G.; Pude, R.; Schulze, M. Comparing Chemical Composition and Lignin Structure of Miscanthus x Giganteus and Miscanthus Nagara Harvested in Autumn and Spring and Separated into Stems and Leaves. *RSC Adv.* **2020**, *10* (18), 10740–10751. https://doi.org/10.1039/C9RA10576J.

(65) Hyväkkö, U.; Maltari, R.; Kakko, T.; Kontro, J.; Mikkilä, J.; Kilpeläinen, P.; Enqvist, E.; Tikka, P.; Hildén, K.; Nousiainen, P.; Sipilä, J. On the Effect of Hot-Water Pretreatment in Sulfur-Free Pulping of Aspen and Wheat Straw. *ACS Omega* **2020**, *5* (1), 265–273. https://doi.org/10.1021/acsomega.9b02619.

(66) Lesage, A.; Bardet, M.; Emsley, L. Through-Bond Carbon−Carbon Connectivities in Disordered Solids by NMR. *J. Am. Chem. Soc.* **1999**, *121* (47), 10987–10993. https://doi.org/10.1021/ja992272b.

(67) Newman, R. H.; Hemmingson, J. A. Carbon-13 NMR Distinction between Categories of Molecular Order and Disorder in Cellulose. *Cellulose* **1995**, *2* (2), 95–110. https://doi.org/10.1007/BF00816383.

(68) Wickholm, K.; Larsson, P. T.; Iversen, T. Assignment of Non-Crystalline Forms in Cellulose I by CP/MAS 13C NMR Spectroscopy. *Carbohydr. Res.* **1998**, *312* (3), 123–129. https://doi.org/10.1016/S0008-6215(98)00236-5.

(69) Bootten, T. J.; Harris, P. J.; Melton, L. D.; Newman, R. H. Solid-state 13C-NMR Spectroscopy Shows That the Xyloglucans in the Primary Cell Walls of Mung Bean (Vigna Radiata L.) Occur in Different Domains: A New Model for Xyloglucan–Cellulose Interactions in the Cell Wall. *J. Exp. Bot.* **2004**, *55* (397), 571–583. https://doi.org/10.1093/jxb/erh065.

(70) Fayon, F.; Massiot, D.; Levitt, M. H.; Titman, J. J.; Gregory, D. H.; Duma, L.; Emsley, L.; Brown, S. P. Through-Space Contributions to Two-Dimensional Double-Quantum J Correlation NMR Spectra of Magic-Angle-Spinning Solids. *J. Chem. Phys.* **2005**, *122* (19), 194313. https://doi.org/10.1063/1.1898219.

(71) Hauser, E. A. What the X-Ray Tells Us of the Structure of Cellulose. *Ind. Eng. Chem.* **1929**, *21* (2), 124–125. https://doi.org/10.1021/ie50230a006.

(72) Sarko, A.; Muggli, R. Packing Analysis of Carbohydrates and Polysaccharides. III. Valonia Cellulose and Cellulose II. *Macromolecules* **1974**, *7* (4), 486–494. https://doi.org/10.1021/ma60040a016.

(73) Wang, T.; Zabotina, O.; Hong, M. Pectin–Cellulose Interactions in the *Arabidopsis* Primary Cell Wall from Two-Dimensional Magic-Angle-Spinning Solid-State Nuclear Magnetic Resonance. *Biochemistry* **2012**, *51* (49), 9846–9856. https://doi.org/10.1021/bi3015532.

(74) Wang, T.; Park, Y. B.; Caporini, M. A.; Rosay, M.; Zhong, L.; Cosgrove, D. J.; Hong, M. Sensitivity-Enhanced Solid-State NMR Detection of Expansin's Target in Plant Cell Walls. *Proc. Natl. Acad. Sci.* **2013**, *110* (41), 16444–16449. https://doi.org/10.1073/pnas.1316290110.

(75) Wang, T.; Salazar, A.; Zabotina, O. A.; Hong, M. Structure and Dynamics of *Brachypodium* Primary Cell Wall Polysaccharides from Two-Dimensional ^{13}C Solid-State Nuclear Magnetic Resonance Spectroscopy. *Biochemistry* **2014**, *53* (17), 2840–2854. https://doi.org/10.1021/bi500231b.

(76) Wang, T.; Williams, J. K.; Schmidt-Rohr, K.; Hong, M. Relaxation-Compensated Difference Spin Diffusion NMR for Detecting 13C–13C Long-Range Correlations in Proteins and Polysaccharides. *J. Biomol. NMR* **2015**, *61* (2), 97–107. https://doi.org/10.1007/s10858-014-9889-0.

(77) Phyo, P.; Wang, T.; Xiao, C.; Anderson, C. T.; Hong, M. Effects of Pectin Molecular Weight Changes on the Structure, Dynamics, and Polysaccharide Interactions of Primary Cell Walls of *Arabidopsis Thaliana* : Insights from Solid-State NMR. *Biomacromolecules* **2017**, *18* (9), 2937–2950. https://doi.org/10.1021/acs.biomac.7b00888.

(78) Keegstra, K.; Talmadge, K. W.; Bauer, W. D.; Albersheim, P. The Structure of Plant Cell Walls. *Plant Physiol.* **1973**, *51* (1), 188–197.

(79) Pauly, M.; Albersheim, P.; Darvill, A.; York, W. S. Molecular Domains of the Cellulose/Xyloglucan Network in the Cell Walls of Higher Plants. *Plant J.* **1999**, *20* (6), 629–639. https://doi.org/10.1046/j.1365-313X.1999.00630.x.

(80) Addison, B.; Stengel, D.; Bharadwaj, V. S.; Happs, R. M.; Doeppke, C.; Wang, T.; Bomble, Y. J.; Holland, G. P.; Harman-Ware, A. E. Selective One-Dimensional 13C–13C Spin-Diffusion Solid-State Nuclear Magnetic Resonance Methods to Probe Spatial Arrangements in Biopolymers Including Plant Cell Walls, Peptides, and Spider Silk. *J. Phys. Chem. B* **2020**, *124* (44), 9870–9883. https://doi.org/10.1021/acs.jpcb.0c07759.

(81) Wang, H.-M.; Ma, C.-Y.; Li, H.-Y.; Chen, T.-Y.; Wen, J.-L.; Cao, X.-F.; Wang, X.-L.; Yuan, T.-Q.; Sun, R.-C. Structural Variations of Lignin Macromolecules from Early Growth Stages of Poplar Cell Walls. *ACS Sustain. Chem. Eng.* **2020**, *8* (4), 1813–1822. https://doi.org/10.1021/acssuschemeng.9b05845.

(82) Happs, R. M.; Addison, B.; Doeppke, C.; Donohoe, B. S.; Davis, M. F.; Harman-Ware, A. E. Comparison of Methodologies Used to Determine Aromatic Lignin Unit Ratios in Lignocellulosic Biomass. *Biotechnol. Biofuels* **2021**, *14* (1), 58. https://doi.org/10.1186/s13068-021-01897-y.

(83) Wan Ishak, W. H.; Rosli, N. A.; Ahmad, I. Influence of Amorphous Cellulose on Mechanical, Thermal, and Hydrolytic Degradation of Poly(Lactic Acid) Biocomposites. *Sci. Rep.* **2020**, *10* (1), 11342. https://doi.org/10.1038/s41598-020-68274-x.

(84) Yao, L.; Yang, H.; Yoo, C. G.; Pu, Y.; Meng, X.; Muchero, W.; Tuskan, G. A.; Tschaplinski, T.; Ragauskas, A. J. Understanding the Influences of Different Pretreatments on Recalcitrance of Populus Natural Variants. *Bioresour. Technol.* **2018**, *265*, 75–81. https://doi.org/10.1016/j.biortech.2018.05.057.

(85) Foston, M.; Samuel, R.; Ragauskas, A. J. 13C Cell Wall Enrichment and Ionic Liquid NMR Analysis: Progress towards a High-Throughput Detailed Chemical Analysis of the Whole Plant Cell Wall. *Analyst* **2012**, *137* (17), 3904–3909. https://doi.org/10.1039/C2AN35344J.

(86) Baig, K. S.; Wu, J.; Turcotte, G. Future Prospects of Delignification Pretreatments for the Lignocellulosic Materials to Produce Second Generation Bioethanol. *Int. J. Energy Res.* **2019**, *43* (4), 1411–1427. https://doi.org/10.1002/er.4292.

(87) Tolbert, A. K.; Ma, T.; Kalluri, U. C.; Ragauskas, A. J. Determining the Syringyl/Guaiacyl Lignin Ratio in the Vessel and Fiber Cell Walls of Transgenic *Populus* Plants. *Energy Fuels* **2016**, *30* (7), 5716–5720. https://doi.org/10.1021/acs.energyfuels.6b00560.

(88) Pauly, M.; Keegstra, K. Plant Cell Wall Polymers as Precursors for Biofuels. *Curr. Opin. Plant Biol.* **2010**, *13* (3), 304–311. https://doi.org/10.1016/j.pbi.2009.12.009.

(89) Kim, K. H.; Dutta, T.; Sun, J.; Simmons, B.; Singh, S. Biomass Pretreatment Using Deep Eutectic Solvents from Lignin Derived Phenols. *Green Chem.* **2018**, *20* (4), 809–815. https://doi.org/10.1039/C7GC03029K.

(90) Lopes, A. M.; Filho, E. X. F.; Moreira, L. R. S. An Update on Enzymatic Cocktails for Lignocellulose Breakdown. *J. Appl. Microbiol.* **2018**, *125* (3), 632–645. https://doi.org/10.1111/jam.13923.

(91) Zhao, W.; Kirui, A.; Deligey, F.; Mentink-Vigier, F.; Zhou, Y.; Zhang, B.; Wang, T. Solid-State NMR of Unlabeled Plant Cell Walls: High-Resolution Structural Analysis without Isotopic Enrichment. *Biotechnol. Biofuels* **2021**, *14* (1), 14. https://doi.org/10.1186/s13068-020-01858-x.

(92) Moiceanu, G.; Paraschiv, G.; Voicu, G.; Dinca, M.; Negoita, O.; Chitoiu, M.; Tudor, P. Energy Consumption at Size Reduction of Lignocellulose Biomass for Bioenergy. *Sustainability* **2019**, *11* (9), 2477. https://doi.org/10.3390/su11092477.

(93) Zhao, X.; Zhang, Y.; Hu, H.; Huang, Z.; Yang, M.; Chen, D.; Huang, K.; Huang, A.; Qin, X.; Feng, Z. Effect of Mechanical Activation on Structure Changes and Reactivity in Further Chemical Modification of Lignin. *Int. J. Biol. Macromol.* **2016**, *91*, 1081–1089. https://doi.org/10.1016/j.ijbiomac.2016.06.074.

(94) Zhai, Q.; Li, F.; Wang, F.; Feng, J.; Jiang, J.; Xu, J. Ultrafine Grinding of Poplar Biomass: Effect of Particle Morphology on the Liquefaction of Biomass for Methyl Glycosides and Phenolics. *Cellulose* **2019**, *26* (6), 3685–3701. https://doi.org/10.1007/s10570-019-02332-0.

(95) Wang, Z.; Zhu, X.; Deuss, Peter. J. The Effect of Ball Milling on Birch, Pine, Reed, Walnut Shell Enzymatic Hydrolysis Recalcitrance and the Structure of the Isolated Residual Enzyme Lignin. *Ind. Crops Prod.* **2021**, *167*, 113493. https://doi.org/10.1016/j.indcrop.2021.113493.

(96) Ptashnyk, M.; Seguin, B. The Impact of Microfibril Orientations on the Biomechanics of Plant Cell Walls and Tissues. *Bull. Math. Biol.* **2016**, *78* (11), 2135–2164. https://doi.org/10.1007/s11538-016-0207-8.

(97) Sun, R.; Mott, L.; Bolton, J. Isolation and Fractional Characterization of Ball-Milled and Enzyme Lignins from Oil Palm Trunk. *J. Agric. Food Chem.* **1998**, *46* (2), 718–723. https://doi.org/10.1021/jf9705532.

(98) Zheng, Y.; Ning, G.; Cosgrove, D. J. High-Resolution Imaging of Cellulose Organization in Cell Walls by Field Emission Scanning Electron Microscopy. In *The Plant Cell Wall: Methods and Protocols*; Popper, Z. A., Ed.; Methods in Molecular Biology; Springer: New York, NY, 2020; pp 225–237. https://doi.org/10.1007/978-1-0716-0621-6_13.

(99) Harris, R. K.; Becker, E. D.; Menezes, S. M. C. D.; Granger, P.; Hoffman, R. E.; Zilm, K. W. Further Conventions for NMR Shielding and Chemical Shifts (IUPAC Recommendations 2008). *Magn. Reson. Chem.* **2008**, *46* (6), 582–598. https://doi.org/10.1002/mrc.2225.

(100) Delaglio, F.; Grzesiek, S.; Vuister, G. W.; Zhu, G.; Pfeifer, J.; Bax, A. NMRPipe: A Multidimensional Spectral Processing System Based on UNIX Pipes. *J. Biomol. NMR* **1995**, *6* (3), 277–293. https://doi.org/10.1007/BF00197809.

(101) Lee, W.; Tonelli, M.; Markley, J. L. NMRFAM-SPARKY: Enhanced Software for Biomolecular NMR Spectroscopy. *Bioinformatics* **2015**, *31* (8), 1325–1327. https://doi.org/10.1093/bioinformatics/btu830.

(102) Yang, H.; Yoo, C. G.; Meng, X.; Pu, Y.; Muchero, W.; Tuskan, G. A.; Tschaplinski, T. J.; Ragauskas, A. J.; Yao, L. Structural Changes of Lignins in Natural Populus Variants during Different Pretreatments. *Bioresour. Technol.* **2020**, *295*, 122240. https://doi.org/10.1016/j.biortech.2019.122240.

(103) Zhao, X.; Huang, Z.; Zhang, Y.; Yang, M.; Chen, D.; Huang, K.; Hu, H.; Huang, A.; Qin, X.; Feng, Z. Efficient Solid-Phase Synthesis of Acetylated Lignin and a Comparison of the Properties of Different Modified Lignins. *J. Appl. Polym. Sci.* **2017**, *134* (1). https://doi.org/10.1002/app.44276.

(104) Li, H.; Foston, M. B.; Kumar, R.; Samuel, R.; Gao, X.; Hu, F.; Ragauskas, A. J.; Wyman, C. E. Chemical Composition and Characterization of Cellulose for Agave as a Fast-Growing, Drought-Tolerant Biofuels Feedstock. *RSC Adv.* **2012**, *2* (11), 4951–4958. https://doi.org/10.1039/C2RA20557B.

(105) Dou, J.; Kim, H.; Li, Y.; Padmakshan, D.; Yue, F.; Ralph, J.; Vuorinen, T. Structural Characterization of Lignins from Willow Bark and Wood. *J. Agric. Food Chem.* **2018**, *66* (28), 7294–7300. https://doi.org/10.1021/acs.jafc.8b02014.

(106) Agarwal, U. P.; Ralph, S. A.; Reiner, R. S.; Baez, C. Probing Crystallinity of Never-Dried Wood Cellulose with Raman Spectroscopy. *Cellulose* **2016**, *23* (1), 125–144. https://doi.org/10.1007/s10570-015-0788-7.

(107) Dinant, S.; Wolff, N.; De Marco, F.; Vilaine, F.; Gissot, L.; Aubry, E.; Sandt, C.; Bellini, C.; Le Hir, R. Synchrotron FTIR and Raman Spectroscopy Provide Unique Spectral Fingerprints for Arabidopsis Floral Stem Vascular Tissues. *J. Exp. Bot.* **2019**, *70* (3), 871–884. https://doi.org/10.1093/jxb/ery396.

(108) Mateu, B. P.; Bock, P.; Gierlinger, N. Raman Imaging of Plant Cell Walls. In *The Plant Cell Wall: Methods and Protocols*; Popper, Z. A., Ed.; Methods in Molecular Biology; Springer: New York, NY, 2020; pp 251–295. https://doi.org/10.1007/978-1-0716-0621-6_15.

(109) Phyo, P.; Gu, Y.; Hong, M. Impact of Acidic PH on Plant Cell Wall Polysaccharide Structure and Dynamics: Insights into the Mechanism of Acid Growth in Plants from Solid-State NMR. *Cellulose* **2019**, *26* (1), 291–304. https://doi.org/10.1007/s10570-018-2094-7.

(110) Zeng, Y.; Zhao, S.; Wei, H.; Tucker, M. P.; Himmel, M. E.; Mosier, N. S.; Meilan, R.; Ding, S.-Y. In Situ Micro-Spectroscopic Investigation of Lignin in Poplar Cell Walls Pretreated by Maleic Acid. *Biotechnol. Biofuels* **2015**, *8* (1), 126. https://doi.org/10.1186/s13068-015-0312-1.

(111) Elena, B.; Lesage, A.; Steuernagel, S.; Böckmann, A.; Emsley, L. Proton to Carbon-13 INEPT in Solid-State NMR Spectroscopy. *J. Am. Chem. Soc.* **2005**, *127* (49), 17296–17302. https://doi.org/10.1021/ja054411x.

(112) Silva, T. N.; Thomas, J. B.; Dahlberg, J.; Rhee, S. Y.; Mortimer, J. C. Progress and Challenges in Sorghum Biotechnology, a Multipurpose Feedstock for the Bioeconomy. *J. Exp. Bot.* **2022**, *73* (3), 646–664. https://doi.org/10.1093/jxb/erab450.

(113) Wang, J.; Feng, J.; Jia, W.; Fan, P.; Bao, H.; Li, S.; Li, Y. Genome-Wide Identification of Sorghum Bicolor Laccases Reveals Potential Targets for Lignin Modification. *Front. Plant Sci.* **2017**, *8*.

Appendix

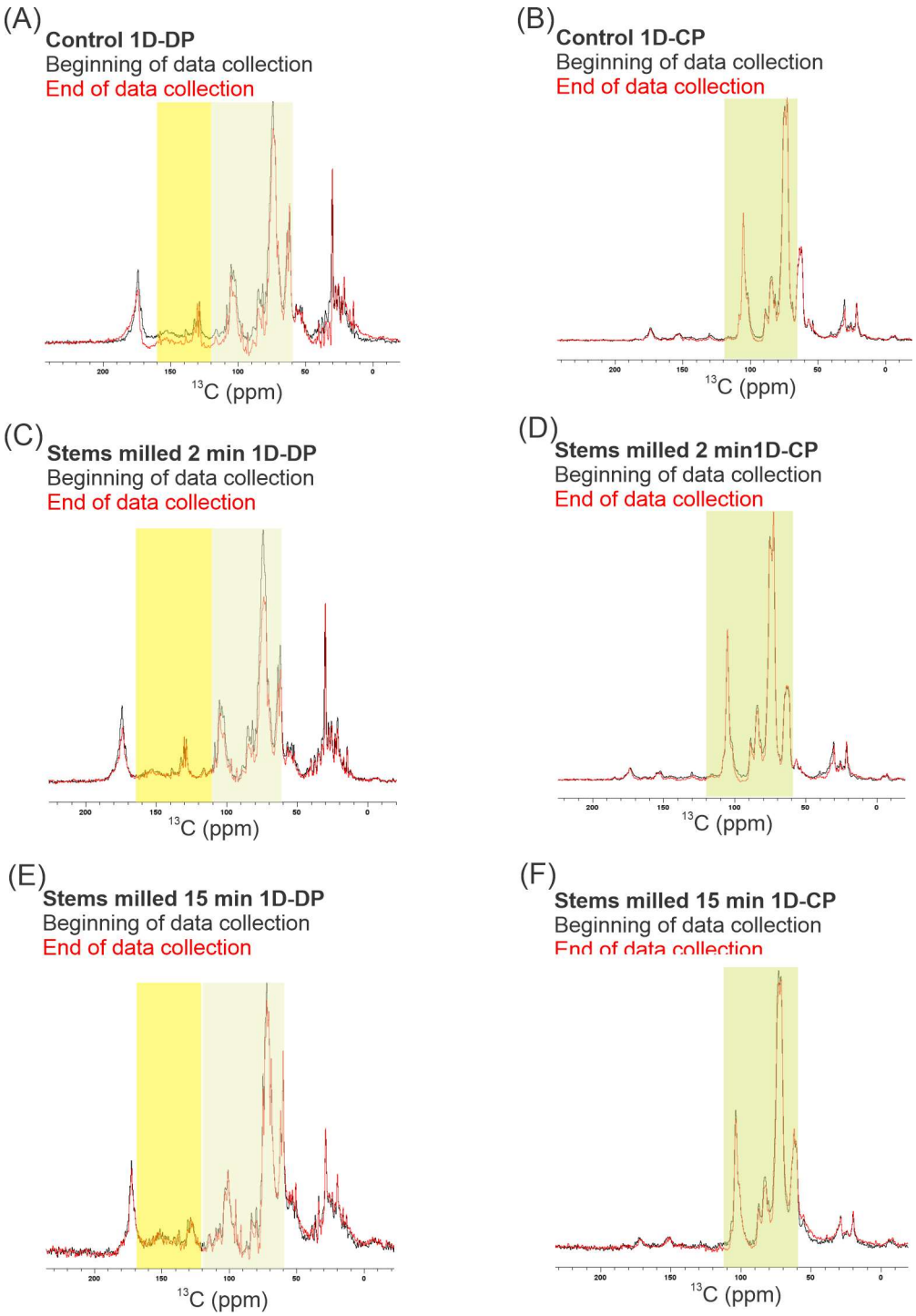

Figure S1. The 1D experiments used to monitor sample degradation during solid-state NMR data collection are presented here for the control 1D DP (A) and 1D CP (B), stems milled for 2 minutes 1D DP (C) and 1D CP (D), and the stems milled for 15 minutes 1D DP (E) and 1D CP (F). The 1D data at the beginning of the data collection are in black and the experiments after the final data collection are presented in red. Minor changes in the 1D DP give information about sample viability given signal changes in the neutral polysaccharide region outlined in green, the lignin region highlighted in yellow is at a signal intensity so

only large changes are noted. Signal reduction does occur overall during solid-state NMR as the sample is irradiated during excitations.

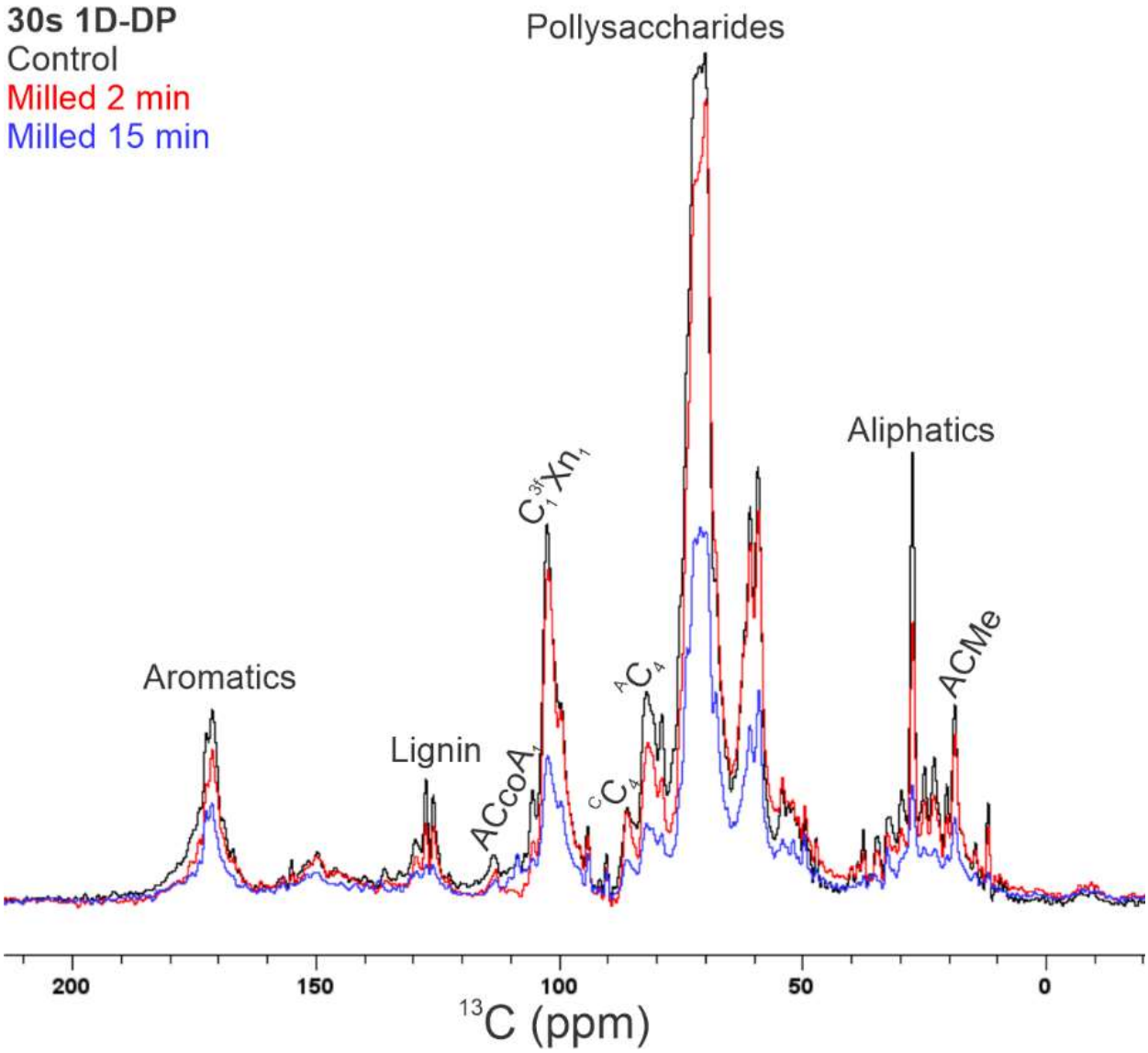

Figure S2. The quantitative 30 s 1D-DP experiments to quantify polymers from the control (black), stems milled for 2 minutes (red), and stems milled for 15 minutes (blue) are overlayed and given general assignments.

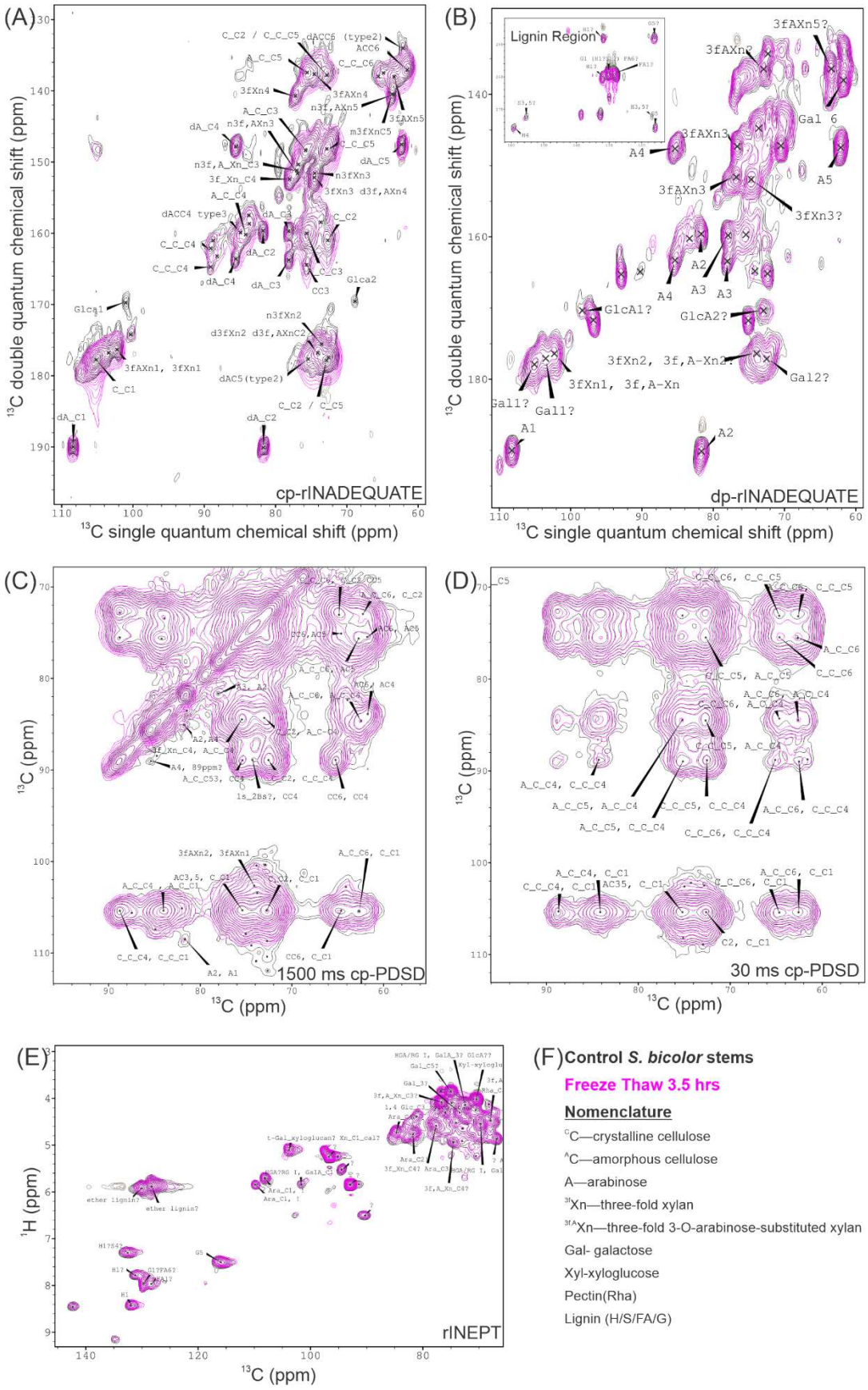

(F) **Control *S. bicolor* stems**

Freeze Thaw 3.5 hrs

Nomenclature

^{C}C—crystalline cellulose

^{A}C—amorphous cellulose

A—arabinose

^{3f}Xn—three-fold xylan

^{3fA}Xn—three-fold 3-O-arabinose-substituted xylan

Gal- galactose

Xyl-xyloglucose

Pectin(Rha)

Lignin (H/S/FA/G)

Figure S3. The comparison between the control (black) and a stem sample which was left to be unthawed for 3.5 hrs in accordance to what stems would be exposed to when mechanically milled for 120 minutes as recommended by Kim and Ralph 2010 for the desired sample size of 600 mg. The experiments selected experiments show no changes in the CP-rINADEQUATE (A), DP-rINADEQUATE polysaccharide and lignin region (B), 30 ms CP-PDSD (C), 1500 ms CP-PDSD (D), and the rINEPT plant cell wall region 160-55 ppm (E). A key is provided for the polymer abbreviations of all the spectra (A-E) in panel F.

Table S1. Below is the table of assignments reproduced from the original characterization of Sorghum bicolor plant cell walls.[24] These values were referenced with a tolerance of 0.5 ppm and by peak position in the spectra for the CP-rINADEQUATE, 30 ms CP-PDSD, 1500 ms CP-PDSD, and the rINEPT given spectra presented in Gao et al. 2020. The unambiguous chemical shifts are highlighted which can be used to identify polymers in overlapped spectra.

	Polysaccharide	**Chemical shift (ppm)**						
Name	**Type, unit (denotation)**	**C1**	**C2**	**C3**	**C4**	**C5**	**C6**	**References/notes**
Cellulose	Crystalline, glucose (^{1C}C)	105.2	72.8	75.1	88.1	72.8	64.8	1–4
	Crystalline, glucose (^{2C}C)	105.2	72.8	75.8	89	72.6	65.4	1–4
	Crystalline, glucose (^{3C}C)	105.2	72.8	75.8	89.5	73	65.3	1–4
	Amorphous, glucose (^{1A}C)	105.2	72.8	75.1	83.8	75.1	61.8	1–4
	Amorphous, glucose (^{2A}C)	105.2	72.8	75.4	84.1	75.4	62.2	1–4
	Amorphous, glucose (^{3A}C)	105.2	72.8	75.8	84.7	75.8	62.5	1–4
Xylan	Two-fold screw, xylose (^{2f}Xn)	105.1	72.3	75.3	82.1	64.1	N/A	1–3
	Three-fold screw, xylose (^{3f}Xn)	102.5	73.7	74.7	77.3	63.8	N/A	1,2
	Three-fold screw, 3-*O*-arbinose-substituted xylose (^{3f,A}Xn)	102.5	74	76.7	74.6	63.6	N/A	4,5
	Arabinose (A)	108.4	81.8	78.2	85.6	62.4	N/A	1,4,6
	Glucuronic acid (GlcA)	98.6	72.4	-	-	-	-	6
	Acetate (AC^{CO}, AC^{Me})	174	21.4	N/A	N/A	N/A	N/A	2

Cellulose superscripts 1--3 correspond to the most hydrated to the least hydrated cellulose polymer chemical shifts previously predicted to correspond to exterior to interior polymers as supported in (Dick-Perez et al. 2011) References contributing to the figure include Terret et al. 2019([1]), Simmons et al. 2016([2]), Kang et al. 2019([3]), Wang et al. 2014([4]), Komatsu et al. 2013 ([5]), and Dick Perez et al. 2011 ([6]).

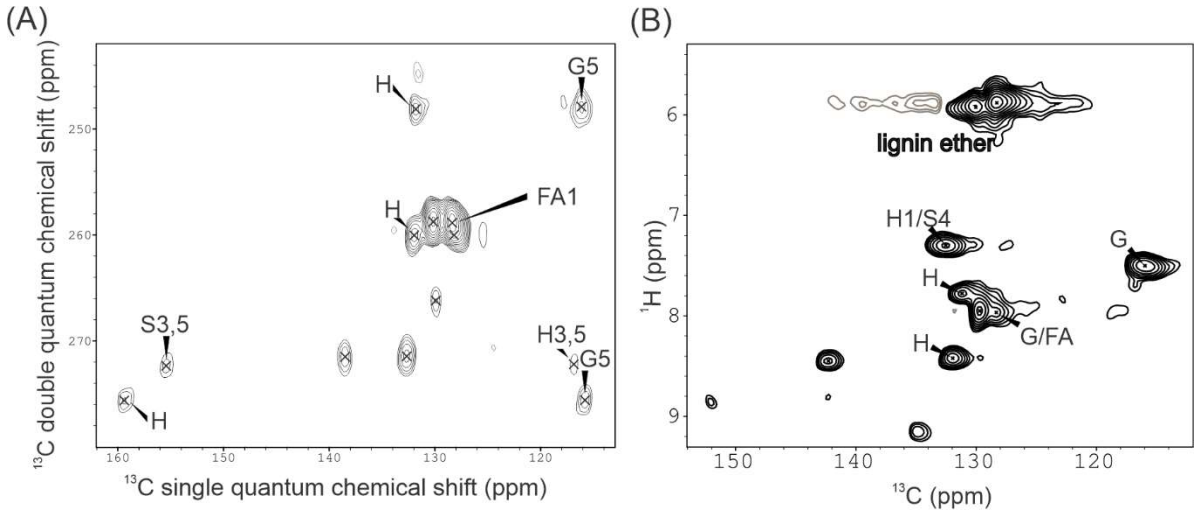

Figure S4. The control stems carbon assignments of lignin from the DP-rINADEQUATE (A) and the lignin peaks from the rINEPT (B) are presented here. Within the SPARKY program consistent carbon chemical shifts could be matched between the DP-rINADEQUATE to the rINEPT

Table S2. Current assignment of the highly dynamic polysaccharides is summarized in the table below from the rINEPT and previous references.[24,34,47,77] The proton assignments discussed in Ding et al. 2011 and Phyo and Hong 2019 correspond to descriptions of the primary plant cell wall but the peaks below are uncharacterized within the pectin region. The assignments 1--5 are for H (top) and C (bottom) in ppm.

Assignment	1	2	3	4	5	6	REF
Hemicellulose							
Arabinose	5.7	4.8	-	-	-	-	[24]
	108.1	81.7					
^{3f} Xn	-	-	-	4.6	4.7	NA	[24,34]
				77.6	61.9		
^{3f,A} Xn	-	-	4.1	4.9	4.2	NA	[24]
			76.6	74.6	63.5		
Pectin							
Arabinose (pectin)	5.8	-	-	4.7	-	NA	[24,34]
	109.8			84.7			
HGA, RGI	-	4.5	-	-	-	-	[28]
		69.7					
RGI,Ara	-	-	-	-	4.5	-	[28,34]
					68.0		
Galactan	5.1	-	4.3	-	3.9	4.4	[28,34]
	103.8		73.5		75.0	61.8	

Table S3. Assignment of lignin from the DP-rINADEQUATE of the stem control was designated from the aromatic rings of monolignols 110--160 pm, within the lignin range described in Wang et al 2020.[81] The following carbons C1--C6 are presented to be within the phenyl ring of monolignols, per convention the C1 position is set by vinyl alcohol/carboxylic acid group. This assignment is initial and may not fully

encapsulate lignin in its heteroaromatic form, consider Figure 4B containing linkages between aromatic groups.

Lignin Assignment	C1	C2	C3	C4	C5	C6
H	131.9	128.4	116.8	159.4	116.8	128.4
	131.8					
G	129.9	-	-	-	115.8	-
	130.2				116.1	
S	138.5	-	155.4	-	155.4	-
FA	128.4	-	-	-	-	129.9
	-					130.2

Table S4. Cursory assignment of lignin from the highly dynamic components presented in the rINEPT from DP-rINADEQUATE assignments and previous lignin assignments on grass within Wang *et al.* 2020 and Table S3. The protons in the table have not been assigned, but are directly bonded to established lignin carbons which are assigned in Table S3. The ether linkage noted by a chemical shift near 6ppm and the unassigned peaks are also presented in this table.

Monolignol	2	5	6	
H	7.967	-	7.967	
	128.3	-	128.3	
G	-	7.501	-	
	-	116.0	-	
FA	-	-	7.95	
	-	-	129.7	
Linkage	X	Y	Z	W
ether lignin	5.925	5.88	-	-
	130.0	128.3	-	-
Other	7.3	7.778	8.42	8.449
	132.5	131.2	131.9	142.3

Table S5. The 1500 ms CP-PDSD experiment integral values of unambiguous cellulose 1 crosspeaks. These peak changes were evaluated from peaks selected from the control and integrated across the control, stems milled for 2 minutes, and stems milled for 15 minutes using NMRPipe. These changes were consistent with the peaks present across the stem data when peaks were picked from the data of the stems milled for 2 minutes and the stems milled for 15 minutes.

Assignment	2min milled peak (relative to control)	error (±0.0001)	15 min milled peak (relative to control)	error (±0.0001)
$^{C}C_4$,C_1	0.9970	0.0159	0.1155	0.0112
$^{A}C_4$,C_1	0.8217	0.0088	0.1016	0.0062
$^{A}C_3$,5 , C_1	0.8865	0.0030	0.1227	0.0021
C_2, C_1	0.8787	0.0026	0.1259	0.0018
$^{C}C_6$,C1	0.9047	0.0090	0.1028	0.0064
$^{A}C_6$, C_1	0.8738	0.0088	0.1271	0.0062

Table S6. The 30 ms CP-PDSD experiment integral values of unambiguous cellulose 1 crosspeaks. These peak changes were evaluated from peaks selected from the control and integrated across the control, stems milled for 2 minutes, and stems milled for 15 minutes using NMRPipe. These changes were consistent with the peaks present across the stem data when peaks were picked from the data of the stems milled for 2 minutes and the stems milled for 15 minutes.

Assignment	2min milled peak (relative to control)	error (±0.0001)	15 min milled peak (relative to control)	error (±0.0001)
$^{C}C_4,C_1$	1.0153	0.0169	0.1377	0.0128
$^{A}C_4,C_1$	0.8791	0.0100	0.1189	0.0076
$^{A}C_3,5$, C_1	0.8807	0.0034	0.1350	0.0026
C_2, C_1	0.8627	0.0023	0.1355	0.0017
$^{C}C_6$,C1	0.8028	0.0136	0.1132	0.0103
$^{A}C_6$, C_1	0.7465	0.0139	0.1147	0.0106

Table S7. The CP-rINADEQUATE experiment integral values of cellulose peaks. These peak changes were evaluated from peaks selected from the control and integrated across the control, stems milled for 2 minutes, and stems milled for 15 minutes using NMRPipe. These changes were consistent with the peaks present across the stem data when peaks were picked from the data of the stems milled for 2 minutes and the stems milled for 15 minutes.

Assignment	2min milled peak (relative to control %)	error (±0.001%)	15 min milled peak (relative to control %)	error (±0.001%)
$^{C}C_{4i}$	0.4974	0.0554	0.0119	0.0329
$^{C}C_{4ii}$	0.8022	0.0352	0.0965	0.0209
$^{C}C_{4iii}$	0.7583	0.0315	0.0781	0.0188
$^{A}C_{4i}$	0.8396	0.0224	0.0434	0.0133
$^{A}C_{4ii}$	0.7579	0.0177	0.0940	0.0105
$^{A}C_{4iii}$	0.8232	0.0170	0.0762	0.0101

Table S8. The CP-rINADEQUATE experiment integral values of hemicellulose peaks. These peak changes were evaluated from peaks selected from the control and integrated across the control, stems milled for 2 minutes, and stems milled for 15 minutes using NMRPipe. These changes were consistent with the peaks present across the stem data when peaks were picked from the data of the stems milled for 2 minutes and the stems milled for 15 minutes.

Assignment	2min milled peak (relative to control %)	error (±0.001%)	15 min milled peak (relative to control %)	error (±0.001%)
A_1	0.4869	0.0074	0.0806	0.0044
A_2	0.5484	0.0073	0.0859	0.0044
A_2	0.5746	0.0142	0.0800	0.0084
A_3	0.5637	0.0133	0.1048	0.0079
A_3	0.3738	0.0204	0.0810	0.0122
A_4	0.5346	0.0218	0.0366	0.0129
A_4	0.5769	0.0130	0.0544	0.0077
A_5	0.5697	0.0081	0.0880	0.0048

$^{3f/3f,A}Xn_1$	0.5923	0.0149	0.0457	0.0089
$^{3f/3f,A}Xn_2$	0.6803	0.0090	0.1325	0.0054
$^{3f}Xn_3$, $^{3f,A}Xn_4$	1.2081	0.0167	0.1811	0.0099
$^{3f}Xn_4$	1.0582	0.0225	0.1740	0.0134
$^{3f,A}Xn_3$	1.1525	0.0195	0.1937	0.0116
$^{3f}Xn_4$	0.6282	0.0126	0.0666	0.0075
$^{3f}Xn_5$	0.4955	0.0385	0.0365	0.0229

Table S9. The rINEPT experiment integral values of hemicellulose and lignin peaks. These peak changes were evaluated from peaks selected from the control and integrated across the control, stems milled for 2 minutes, and stems milled for 15 minutes using NMRPipe. These changes were consistent with the peaks present across the stem data when peaks were picked from the data of the stems milled for 2 minutes and the stems milled for 15 minutes.

Assignment	2min milled peak (relative to control %)	error (±0.001%)	15 min milled peak (relative to control %)	error (±0.001%)
$A_{1,hemicellulose}$	0.3935	0.0392	0.1481	0.0223
$A_{1,pectin}$	0.2962	0.0162	0.0569	0.0092
lignin ether (1)	0.1110	0.0099	0.0064	0.0057
lignin ether (2)	0.1175	0.0064	0.0031	0.0037
H_x	0.2906	0.0230	0.3869	0.0131
H_y	0.1599	0.0253	0.1401	0.0144
H_1,S_4	0.2571	0.0197	0.2165	0.0112
G	0.2281	0.0151	0.1982	0.0086

Table S10. CP-rINADEQUATE assignments from the control. These peak changes were evaluated from peaks selected from the control and integrated across the control, stems milled for 2 minutes, and stems milled for 15 minutes using NMRPipe. The 2D chemical shifts of the SQ and DQ chemical shifts is in ppm. Volume of the 2D data integrated (VOL) is normalized to the first dataset, the control (Z_A0), and the data from the stems milled for 2 minutes (Z_A1) and 15 minutes (Z_A2). The error for the control (Z_A0_err), stems milled for 2 minutes (Z_A1_err) and 15 minutes (Z_A2_err) from the power spectra of the corresponding data collection is scaled to the peak volume and the relative intensity of the control for all peaks.

SQ (ppm)	DQ (ppm)	VOL	Z_A0	Z_A1	Z_A2	Z_A0_err	Z_A1_err	Z_A2_err
108.367	190.005	4.350E+08	1	0.5584	0.1642	0.007482	0.008469	0.008946
81.693	190.061	4.389E+08	1	0.6289	0.1750	0.007415	0.008394	0.008866
81.717	159.567	2.262E+08	1	0.6589	0.1628	0.014387	0.016285	0.017201
78.124	159.626	2.423E+08	1	0.6465	0.2134	0.01343	0.015202	0.016058
78.124	163.655	1.572E+08	1	0.4287	0.1649	0.0207	0.023432	0.02475
85.572	163.538	1.476E+08	1	0.6131	0.0746	0.022054	0.024964	0.026368
85.554	147.738	2.466E+08	1	0.6616	0.1107	0.013196	0.014937	0.015778
62.279	147.624	3.956E+08	1	0.6533	0.1792	0.008227	0.009312	0.009836
173.741	195.016	2.411E+08	1	1.0037	0.1952	0.0135	0.015281	0.016141

174.325	195.771	2.279E+08	1	0.7135	0.1234	0.014279	0.016163	0.017072
173.991	195.366	2.420E+08	1	0.9824	0.1872	0.013448	0.015222	0.016079
21.381	195.246	4.321E+08	1	0.8824	0.1693	0.007532	0.008525	0.009005
105.151	177.683	9.827E+08	1	0.9187	0.1257	0.003312	0.003748	0.003959
72.737	177.714	5.740E+08	1	0.9525	0.1344	0.00567	0.006418	0.006779
72.677	160.945	1.363E+08	1	1.0568	0.1752	0.023884	0.027035	0.028556
72.861	148.287	4.056E+08	1	0.9092	0.0920	0.008024	0.009083	0.009594
89.103	164.849	5.948E+07	1	0.9497	0.1789	0.054711	0.06193	0.065414
75.619	164.514	6.534E+07	1	1.3595	0.1868	0.049807	0.056378	0.05955
88.613	160.945	9.127E+07	1	0.9200	0.1965	0.035657	0.040362	0.042633
89.011	162.005	1.018E+08	1	0.8696	0.1590	0.031954	0.03617	0.038205
87.295	159.886	5.802E+07	1	0.5704	0.0243	0.056093	0.063495	0.067066
84.813	159.942	1.889E+08	1	0.9441	0.1551	0.017226	0.019499	0.020596
84.261	160.221	1.815E+08	1	0.8692	0.1915	0.017928	0.020294	0.021435
83.587	158.882	1.433E+08	1	0.9628	0.0884	0.022704	0.025699	0.027145
73.627	158.38	1.025E+08	1	0.8825	0.2544	0.031755	0.035944	0.037966
75.558	160.221	2.676E+08	1	0.9976	0.1107	0.012163	0.013768	0.014542
75.68	148.399	4.226E+08	1	0.8750	0.0985	0.007702	0.008718	0.009208
75.524	137.392	3.044E+08	1	0.7730	0.0985	0.010693	0.012103	0.012784
72.754	137.649	1.505E+08	1	0.9104	0.2224	0.021618	0.024471	0.025847
64.731	137.723	1.363E+08	1	0.6961	0.0701	0.023869	0.027018	0.028538
65.379	138.091	1.099E+08	1	0.7262	0.0948	0.029616	0.033523	0.035409
61.458	136.95	3.309E+08	1	0.9633	0.1551	0.009836	0.011134	0.01176
101.037	169.7	7.493E+07	1	0.3139	0.0838	0.043433	0.049164	0.05193
68.86	169.519	5.230E+07	1	0.4158	0.0647	0.06222	0.07043	0.074392
102.209	176.36	3.898E+08	1	0.9980	0.2564	0.00835	0.009451	0.009983
73.98	176.857	4.346E+08	1	0.7932	0.2084	0.007488	0.008476	0.008952
75.333	177.946	2.155E+08	1	0.6792	0.0931	0.0151	0.017093	0.018054
74.496	152.252	3.571E+08	1	0.7802	0.2697	0.009114	0.010316	0.010896
77.949	152.375	2.577E+08	1	0.6356	0.2477	0.012631	0.014297	0.015102
77.095	151.465	1.921E+08	1	1.3854	0.3687	0.01694	0.019175	0.020254
77.179	140.607	1.425E+08	1	1.2135	0.3542	0.022838	0.025851	0.027305
63.569	140.544	1.650E+08	1	1.3217	0.3945	0.019718	0.022319	0.023575
63.192	138.208	2.545E+08	1	0.7204	0.1357	0.012785	0.014472	0.015286
75.33	155.082	8.340E+07	1	0.5682	0.0744	0.03902	0.044168	0.046653
79.488	154.774	6.692E+07	1	0.4210	-0.0244	0.048631	0.055047	0.058144
103.453	176.858	3.926E+08	1	0.8704	0.1798	0.008289	0.009383	0.009911

Table S11. The 30 ms CP-PDSD integrated peaks from the control. These peak changes were evaluated from peaks selected from the control and integrated across the control, stems milled for 2 minutes, and stems milled for 15 minutes using NMRPipe. The 2D chemical shifts of the directly detected dimension SQ_{dir} and and the indirectly detected dimension SQ_{ind} chemical shifts is in ppm. Volume of the 2D data integrated (VOL) is normalized to the first dataset, the control (Z_A0), and the data from the stems milled

for 2 minutes (Z_A1) and 15 minutes (Z_A2). The error for the control (Z_A0_err), stems milled for 2 minutes (Z_A1_err) and 15 minutes (Z_A2_err) from the power spectra of the corresponding data collection is scaled to the peak volume and the relative intensity of the control for all peaks.

SQ_{dir}	SQ_{ind}	VOL	Z_A0	Z_A1	Z_A2	Z_A0_err	Z_A1_err	Z_A2_err
108.53	81.626	4.0288E+07	1	0.7761	0.0236	0.042444	0.061636	0.082953
89.043	85.347	3.7112E+07	1	0.672	0.3195	0.046077	0.066911	0.090052
85.139	81.757	5.4538E+07	1	0.7108	0.3221	0.031354	0.045531	0.061278
81.699	78.026	1.2208E+08	1	0.7615	0.3071	0.014007	0.020341	0.027376
105.497	75.273	6.3799E+08	1	1.01	0.2749	0.00268	0.003892	0.005238
105.466	72.787	9.5839E+08	1	0.9894	0.2759	0.001784	0.002591	0.003487
105.497	64.673	1.5964E+08	1	0.9207	0.2305	0.010712	0.015555	0.020934
105.434	62.623	1.5527E+08	1	0.8561	0.2335	0.011013	0.015992	0.021523
105.466	88.665	1.2826E+08	1	1.1643	0.2804	0.013332	0.01936	0.026056
105.466	83.954	2.1577E+08	1	1.0082	0.2421	0.007925	0.011509	0.015489
102.595	74.163	1.5095E+08	1	0.8843	0.3021	0.011328	0.01645	0.022139
102.469	102.008	1.0602E+09	1	0.9022	0.295	0.001613	0.002342	0.003152
88.99	75.512	1.7412E+08	1	1.1277	0.3297	0.009821	0.014261	0.019194
89.071	74.129	1.5484E+08	1	1.0684	0.3784	0.011044	0.016038	0.021584
89.031	72.52	3.1599E+08	1	1.1224	0.3253	0.005412	0.007858	0.010576
84.425	75.427	4.6785E+08	1	1.0031	0.2684	0.003655	0.005308	0.007143
84.505	72.887	3.9956E+08	1	0.9254	0.2639	0.00428	0.006215	0.008364
88.99	65.238	1.3324E+08	1	1.122	0.3019	0.012834	0.018637	0.025082
84.706	62.415	1.9841E+08	1	0.941	0.2773	0.008619	0.012516	0.016844
84.105	61.738	1.9515E+08	1	0.9755	0.2667	0.008762	0.012724	0.017125
72.932	64.899	5.0948E+08	1	0.9634	0.2612	0.003356	0.004874	0.00656
75.495	62.726	5.0989E+08	1	0.9598	0.2761	0.003354	0.00487	0.006554

Table S12. The 1500 ms CP-PDSD integrated peaks from the control. These peak changes were evaluated from peaks selected from the control and integrated across the control, stems milled for 2 minutes, and stems milled for 15 minutes using NMRPipe. The 2D chemical shifts of the directly detected dimension SQ_{dir} and and the indirectly detected dimension SQ_{ind} chemical shifts is in ppm. Volume of the 2D data integrated (VOL) is normalized to the first dataset, the control (Z_A0), and the data from the stems milled for 2 minutes (Z_A1) and 15 minutes (Z_A2). The error for the control (Z_A0_err), stems milled for 2 minutes (Z_A1_err) and 15 minutes (Z_A2_err) from the power spectra of the corresponding data collection is scaled to the peak volume and the relative intensity of the control for all peaks.

SQ_{dir}	SQ_{ind}	VOL	Z_A0	Z_A1	Z_A2	Z_A0_err	Z_A1_err	Z_A2_err
105.456	88.71	1.011E+08	1	1.1434	0.2351	0.011204	0.01825	0.022898
105.406	84.035	1.822E+08	1	0.9423	0.2068	0.006215	0.010124	0.012702
105.505	64.728	1.789E+08	1	1.0375	0.2094	0.006331	0.010313	0.012939
105.456	62.587	1.822E+08	1	1.0021	0.2588	0.006216	0.010125	0.012704
105.335	75.341	5.329E+08	1	1.0166	0.2498	0.002125	0.003462	0.004344
105.366	72.671	6.252E+08	1	1.0077	0.2563	0.001812	0.002951	0.003703

88.973	75.204	1.491E+08	1	1.119	0.2991	0.007599	0.012378	0.01553
88.827	72.522	1.776E+08	1	1.1359	0.3059	0.006377	0.010388	0.013034
84.452	75.304	2.643E+08	1	0.9751	0.2174	0.004286	0.006981	0.008759
84.489	72.772	3.068E+08	1	0.9834	0.23	0.003691	0.006013	0.007544
84.27	64.676	9.055E+07	1	0.9314	0.1476	0.012509	0.020376	0.025565
84.452	62.846	8.991E+07	1	1.0105	0.231	0.012597	0.020519	0.025745
87.842	64.877	4.845E+07	1	1.0035	0.1047	0.023377	0.03808	0.047779
89.009	62.495	4.617E+07	1	1.0904	0.2886	0.024534	0.039963	0.050142
88.936	65.052	4.956E+07	1	1.4031	0.3725	0.022852	0.037225	0.046706
73.005	64.676	2.984E+08	1	1.0019	0.2626	0.003796	0.006184	0.007759
73.042	62.696	3.073E+08	1	1.0054	0.2428	0.003685	0.006003	0.007532
75.411	64.801	2.655E+08	1	1.0113	0.2453	0.004267	0.00695	0.00872
75.484	62.721	2.706E+08	1	0.9994	0.2407	0.004186	0.006818	0.008555

Table S13. The rINEPT integrated peaks from the control. These peak changes were evaluated from peaks selected from the control and integrated across the control, stems milled for 2 minutes, and stems milled for 15 minutes using NMRPipe. The 2D chemical shifts of the directly detected dimension SQ_{dir} and and the indirectly detected dimension SQ_{ind} chemical shifts is in ppm. Volume of the 2D data integrated (VOL) is normalized to the first dataset, the control (Z_A0), and the data from the stems milled for 2 minutes (Z_A1) and 15 minutes (Z_A2). The error for the control (Z_A0_err), stems milled for 2 minutes (Z_A1_err) and 15 minutes (Z_A2_err) from the power spectra of the corresponding data collection is scaled to the peak volume and the relative intensity of the control for all peaks.

SQ_{dir}	SQ_{ind}	VOL	Z_A0	Z_A1	Z_A2	Z_A0_err	Z_A1_err	Z_A2_err
8.855	152.239	2.452E+07	1	0.2638	0.1438	0.050948	0.103405	0.104533
9.154	135.102	4.003E+07	1	0.2452	0.1044	0.031214	0.063352	0.064043
8.455	142.665	6.138E+07	1	0.1148	0.2493	0.020355	0.041313	0.041763
8.419	132.14	9.626E+07	1	0.3333	0.7878	0.01298	0.026344	0.026631
7.78	131.241	8.752E+07	1	0.1834	0.2852	0.014276	0.028975	0.029291
7.97	128.331	3.983E+07	1	0.382	0.283	0.031369	0.063667	0.064361
7.947	129.76	1.610E+08	1	0.275	0.2031	0.007763	0.015755	0.015927
7.298	132.669	1.120E+08	1	0.2948	0.4409	0.011151	0.022633	0.02288
7.505	116.166	1.462E+08	1	0.2616	0.4036	0.008545	0.017344	0.017533
5.879	128.532	3.443E+08	1	0.1348	0.0063	0.003629	0.007365	0.007446
5.904	130.124	2.226E+08	1	0.1273	0.013	0.005613	0.011392	0.011516
5.853	109.89	5.647E+07	1	0.4513	0.3016	0.022125	0.044905	0.045394
5.702	108.177	1.368E+08	1	0.3397	0.1158	0.009131	0.018533	0.018735
5.1	103.956	1.023E+08	1	0.5103	0.4397	0.012216	0.024794	0.025065
5.845	101.741	4.233E+07	1	0.2411	0.3689	0.029518	0.059911	0.060564
6.501	102.911	2.802E+07	1	0.1613	0.1354	0.044594	0.09051	0.091497
6.878	85.735	1.721E+07	1	0.3586	0.1411	0.072592	0.147335	0.148942
6.51	90.123	6.862E+07	1	0.1941	0.3121	0.018207	0.036953	0.037356
5.535	94.595	8.803E+07	1	0.1392	0.1952	0.014194	0.028808	0.029122

5.84	92.965	6.855E+08	1	0.273	0.3266	0.001823	0.0037	0.00374
5.251	96.726	9.220E+08	1	0.3134	0.3699	0.001355	0.00275	0.00278
4.719	84.69	1.672E+08	1	0.3768	0.2392	0.007474	0.015169	0.015335
4.757	81.681	2.143E+08	1	0.4272	0.1758	0.00583	0.011833	0.011962
4.389	81.138	6.310E+07	1	0.6344	0.266	0.019801	0.040189	0.040628
4.824	82.977	1.232E+08	1	0.3473	0.158	0.010141	0.020582	0.020807
4.878	85.275	4.949E+07	1	0.7739	0.3528	0.025244	0.051236	0.051795
4.586	77.674	2.191E+08	1	0.4801	0.2026	0.005702	0.011574	0.0117
4.939	74.53	8.447E+07	1	0.3323	0.3214	0.014792	0.030022	0.030349
4.861	66.72	1.302E+08	1	0.2264	0.2033	0.009596	0.019477	0.019689
4.304	75.849	2.601E+08	1	0.3635	0.2234	0.004803	0.009748	0.009854
3.86	76.711	8.591E+07	1	0.5565	0.2042	0.014544	0.029519	0.029841
4.109	74.936	1.104E+08	1	0.6733	0.5639	0.011319	0.022974	0.023225
4.077	76.711	1.217E+09	1	0.3349	0.3896	0.001027	0.002083	0.002106
3.853	75.037	5.416E+08	1	0.3335	0.3896	0.002307	0.004682	0.004733
4.138	72.4	5.373E+08	1	0.4063	0.3792	0.002325	0.004719	0.004771
4.018	70.371	9.516E+08	1	0.3526	0.42	0.001313	0.002665	0.002694
4.307	73.364	5.717E+08	1	0.5065	0.4011	0.002185	0.004436	0.004484
4.534	69.661	5.681E+08	1	0.4016	0.2862	0.002199	0.004464	0.004513